



Cite as  
Nano-Micro Lett.  
(2019) 11:16

Received: 11 December 2018  
Accepted: 21 January 2019  
Published online: 27 February 2019  
© The Author(s) 2019

## Lead-Free Halide Double Perovskite Materials: A New Superstar Toward Green and Stable Optoelectronic Applications

Liang Chu<sup>1,2</sup>, Waqar Ahmad<sup>3</sup>, Wei Liu<sup>2</sup>, Jian Yang<sup>2</sup>, Rui Zhang<sup>2</sup>, Yan Sun<sup>1</sup>, Jianping Yang<sup>1</sup> ✉, Xing'ao Li<sup>1,2</sup> ✉

✉ Jianping Yang, yangjp@njupt.edu.cn; Xing'ao Li, iamxali@njupt.edu.cn

<sup>1</sup> New Energy Technology Engineering Laboratory of Jiangsu Province & School of Science, Nanjing University of Posts and Telecommunications (NJUPT), Nanjing 210023, People's Republic of China

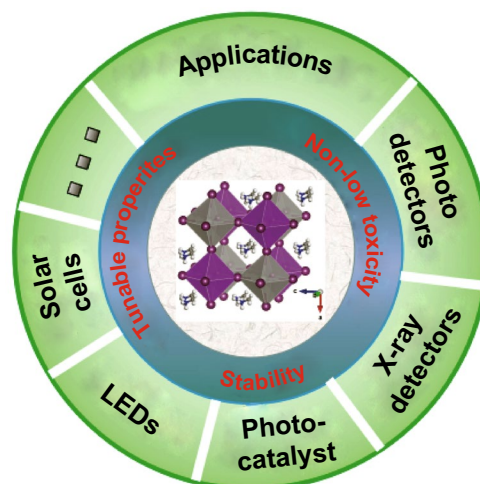
<sup>2</sup> Key Laboratory for Organic Electronics & Information Displays & Institute of Advanced Materials, Jiangsu National Synergistic Innovation Center for Advanced Materials, School of Materials Science and Engineering, Nanjing University of Posts and Telecommunications (NJUPT), Nanjing 210023, People's Republic of China

<sup>3</sup> Wuhan National Laboratory for Optoelectronics (WNLO), Huazhong University of Science and Technology (HUST), Wuhan 430074, People's Republic of China

### HIGHLIGHTS

- Lead-based halide perovskite materials have revealed excellent properties in optoelectronic applications. However, the material stability and the toxicity of lead still hinder their large-scale commercial applications.
- Lead-free halide double perovskite materials possess the characteristics of environmental friendliness, exceptional stability and tunable optoelectronic properties.
- A limited number of halide double perovskites have been synthesized, and extremely few have been developed for optoelectronic applications. Continuing effort is needed to explore more halide double perovskites and modulate the properties for their further applications.

**ABSTRACT** Lead-based halide perovskites have emerged as excellent semiconductors for a broad range of optoelectronic applications, such as photovoltaics, lighting, lasing and photon detection. However, toxicity of lead and poor stability still represent significant challenges. Fortunately, halide double perovskite materials with formula of  $A_2M(I)M(III)X_6$  or  $A_2M(IV)X_6$  could be potentially regarded as stable and green alternatives for optoelectronic applications, where two divalent lead ions are substituted by combining one monovalent and one trivalent ions, or one tetravalent ion. Here, the article provides an up-to-date review on the developments of halide double perovskite materials and their related optoelectronic applications including photodetectors, X-ray detectors, photocatalyst, light-emitting diodes and solar cells. The synthesized halide double perovskite materials exhibit exceptional stability, and a few possess superior optoelectronic properties. However, the number of synthesized halide double perovskites is limited, and more limited materials have been developed for optoelectronic applications to date. In addition, the band structures and carrier transport properties of the materials are still not desired, and



the films still manifest low quality for photovoltaic applications. Therefore, we propose that continuing efforts are needed to develop more halide double perovskites, modulate the properties and grow high-quality films, with the aim of opening the wild practical applications.

**KEYWORDS** Halide double perovskite; Optoelectronic applications; Efficiency; Stability; Toxicity

## 1 Introduction

Halide perovskites with the generic formula  $AM(II)X_3$  ( $A$ :  $CH_3NH_3^+$ ,  $CH(NH_2)_2^+$ ,  $Cs^+$ ;  $M(II)$ :  $Pb^{2+}$ ,  $Sn^{2+}$ ;  $X$ :  $I^-$ ,  $Br^-$ ,  $Cl^-$ ) can be divided into two broad categories according to the A-location cation: organic–inorganic hybrid and all-inorganic halide perovskites. Initially, halide perovskites of  $CH_3NH_3PbX_3$  ( $X=Br, I$ ) were utilized as light sensitizer to replace dyes in dye-sensitized solar cells with liquid electrolyte in 2009 [1]. However, due to the underdeveloped efficiency  $\sim 3.8\%$  and stability, the initial perovskite solar cells (PSCs) did not capture widespread attention. Until 2012, a solid hole transport layer was substituted for the liquid electrolyte to develop all-solid-state PSCs. Most strikingly, the efficiency and stability were simultaneously distinctly improved [2], which stimulated “perovskite fever” [3–5]. Recently, the certified efficiency of PSCs has risen to 23.7%, which is comparable to conventional silicon solar cells [6]. The rocketing improvement of efficiency is attributed to the suitable direct bandgap, strong absorption coefficient, long-range charge diffusion length, balanced electron–hole mobility, high dielectric constant, excellent carrier mobility and small exciton binding energy of halide perovskites [7–10]. Besides solar cells, these materials have been applied in other optoelectronic applications, such as light-emitting diodes (LEDs) [11, 12], lasers [13], photodetectors [14, 15] and X-ray detectors [16].

Although efficiency of PSCs has been progressively grown, there are still huge barriers which limit the commercial applications. For instance, the long-term stability over 10 years is the most critical obstacle to restrict the commercialization [17]. Currently, the PSCs cannot remain stable more than 1 year outdoors, whereas silicon solar cells are usually guaranteed to work for at least 25 years. Moisture, temperature, oxygen and extreme light levels all cause PSCs to decompose. Moisture is the worst problem because reaction with the water forms hydrates to destroy the crystal structures [18]. To improve the stability of PSCs, six main solutions have been adopted: (1) regulating the crystal structures to improve phase stability by doping [19], (2) reducing crystal defects to limit penetrating channels from external

environment [20, 21], (3) designing new stable halide perovskite materials [22, 23], (4) using stable inorganic charge transport layers [24], (5) adopting 2D halide perovskite materials [25, 26] and (6) packaging the devices [27]. Based on the above solutions, cell lifetimes have extended from a few days to months. Nevertheless, there is still a long way to go toward long-time stability over tens of years. Also, toxic lead is still necessary to achieve high performance. Lead pollution will do serious harm to human health, such as fatigue, muscle weakness, clumsiness and clouded consciousness [28]. Extensive efforts have been paid to design new non-/low-toxic and stable halide perovskites for solar cells as well as other optoelectronic applications [29–31].  $Sn^{2+}$  and  $Ge^{2+}$  ions could be expected to replace  $Pb^{2+}$  ions in perovskites. However, the  $Sn^{2+}$  and  $Ge^{2+}$  cations tend to undergo oxidation due to the high-energy-lying 5 s orbitals, rendering the corresponding perovskite extremely unstable in ambient atmosphere [30, 31]. Similarly,  $Bi^{3+}$  and  $Sb^{3+}$  ions with the similar isoelectronic structure have been substituted for  $Pb^{2+}$  ions to develop stable and lead-free perovskites. However, inherently low-dimensional structures of the  $A_3M(III)_2X_9$  perovskites result in less impressive performance [22, 23]. Afterward, doping bivalent metal ions in moderation not only decreases lead content, but also enhances the efficiency and stability, such as  $Sr^{2+}$  [32],  $Co^{2+}$  [33] and  $Zn^{2+}$  [34]. The main reason is that the metal ion-based doping can moderately improve the quality of perovskite films. Simultaneously, doping a certain type of heterovalent metal ions can engineer the band structure of perovskite to enhance the performance, such as  $Ag^+$  [35],  $Sb^{3+}$  [36] and  $Bi^{3+}$  [37]. However, the doping method cannot thoroughly solve any issues of stability or toxicity.

Recently, halide double perovskites ( $A_2M(I)M(III)X_6$ ,  $A_2M(IV)X_6$ ) have been proposed as stable and green alternatives to lead halide perovskites, where two toxic lead ions are substituted by combining one monovalent and one trivalent ions, or one tetravalent ion and one vacancy site (marked as “□”) to yield the same overall charge balance as the conventional perovskites, as shown in Fig. 1a [38]. The formula of  $A_2M(IV)X_6$  is considered as vacancy-ordered halide double perovskites, which is the analogy of  $A_2M(I)$

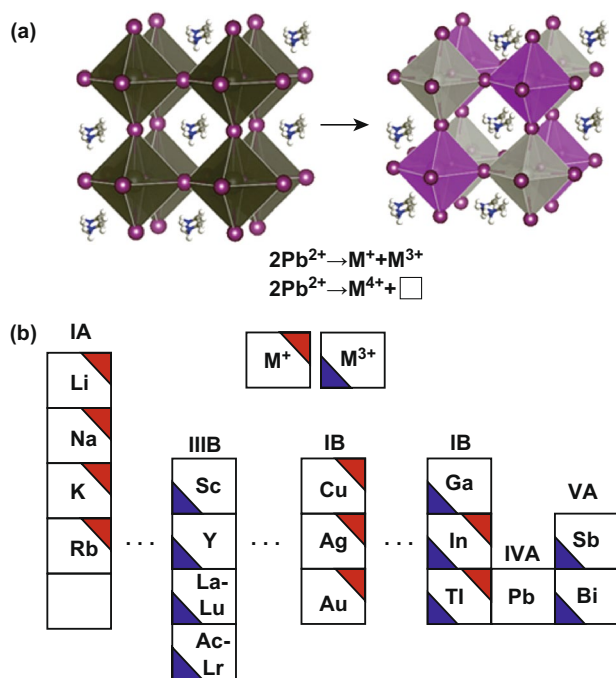


**Fig. 1** **a** Schematic illustration of the transformation from  $\text{APbX}_3$  to  $\text{A}_2\text{M(III)X}_6$  or  $\text{A}_2\text{M(IV)X}_6$ , where two toxic  $\text{Pb}^{2+}$  ions are substituted by combining  $\text{M}^+$  and  $\text{M}^{3+}$  ions (or  $\text{M}^{4+}$  ion). “□” denotes M-site vacancy. **b** Elements of M-location cations with  $\text{M}^+$  and  $\text{M}^{3+}$  in the periodic table for halide double perovskites. When any M-site elements are localized at IA or IIIA groups of the periodic table, the materials have direct bandgaps

$\text{M(III)X}_6$ . Because of the cubic structure ( $\overline{\text{Fm}}\overline{3}\text{m}$ ) to extend three dimensions with corner-sharing metal halide octahedra, halide double perovskites have attracted extensive attention as promising optoelectronic candidates. In this review, we highlight lead-free halide double perovskite materials and their related optoelectronic applications including photodetectors, X-ray detectors, photocatalyst, LEDs and solar cells. The synthesized halide double perovskites exhibited pleasurable stability. But only a limited number of halide double perovskites have been synthesized, and extremely few have been developed for optoelectronic applications. In addition, the band structures and carrier transport properties of the materials are still not desired, and the films still manifest low quality for photovoltaic applications. It is universally acknowledged that significant effort is needed to discover more candidates and modulate the properties for their further applications.

## 2 Halide Double Perovskite Materials

Besides stability, the band structures and carrier transport properties of the materials predetermine to a large extent the specific applications and their performance. In halide perovskites with the chemical formula  $\text{APbX}_3$ , the valence and conduction bands are predominantly made up of the  $\text{Pb-6p}$  and  $\text{X-5p}$  orbitals. In addition, the size of the A-location cation affects the  $\text{PbX}_6$  octahedra to distort/tilt, which can slightly modify the band structures [39]. Similarly, the band structures of the halide double perovskites are mainly decided by the  $\text{M(I)-}$ ,  $\text{M(III)-}$  (or  $\text{M(IV)-}$ ) and X-site atoms. The elements of M-location cations with monovalent and trivalent in the periodic table toward halide double perovskites are shown in Fig. 1b. The elements in IA, IB and IIIA groups can occupy the  $\text{M}^+$  sites, and the elements in IIB, IIIA and VA groups are found at the  $\text{M}^{3+}$  sites. When any M-site elements of the halide double perovskites are localized at IA or IIIA groups of the periodic table, the materials have direct bandgaps. The In and Tl elements in IIIA group possess valencies +1 and +3. The vacancy-ordered halide double perovskites ( $\text{A}_2\text{M(IV)X}_6$ ) all have direct bandgaps. Theoretically, there are a lot of halide double perovskites, though the exact formula must be considered two aspects of the Goldschmidt's rule and thermodynamic stability [40]. However, only a limited number of halide double perovskites have been synthesized so far, as listed in Table 1 including their synthetic methods, where MA is  $\text{CH}_3\text{NH}_3$ .

### 2.1 All-Inorganic Halide Double Perovskites

Initially, all-inorganic halide double perovskite of  $\text{Cs}_2\text{NaAmCl}_6$  was prepared in 1968 by evaporating HCl solution containing cations to dryness [41]. Afterward, a few all-inorganic halide double perovskites ( $\text{Cs}_2\text{NaM(III)Cl}_6$ ) were fabricated by the same method [42–44]. In those days, ferroelectric phase transition was considered particularly attracted for all-inorganic halide double perovskites [45–47], which was observed on the cooling  $\text{Cs}_2\text{NaBiCl}_6$  [47].

In light of the obsessive interest in halide perovskites, halide double perovskites have attained great concern in recent 2 years. In 2016, three different groups almost simultaneously reported  $\text{Cs}_2\text{AgBiX}_6$  ( $\text{X}=\text{Cl}$  or  $\text{Br}$ ) as a promising alternative to the lead halide perovskites, which crystallizes

**Table 1** Summary of the prepared halide double perovskites

Materials	Morphology	Synthetic method	References
$\text{Cs}_2\text{NaMCl}_6$ (M=Am, Bk, Tl, Bi, Lu, etc.)	Powder or single crystal	Evaporating HCl solution to dryness, or heating anhydrous chlorides, or precipitating from cold HCl solution, or growing crystals from dilute HCl solution by cooling evaporation	[41–47]
$\text{Cs}_2\text{AgBiCl}_6$	Powder	Melt crystallization Precipitation from heated acid solution	[48, 49]
	Nanocrystal	Hot injection Antisolvent recrystallization	[50, 51]
$\text{Cs}_2\text{AgBiBr}_6$	Powder	Melt crystallization Precipitation from heated acid solution	[48]
	Single crystal	Cooling crystallization	[52, 54, 55]
	Nanocrystal	Hot injection Antisolvent recrystallization	[50, 51, 56]
$\text{Cs}_2(\text{Ag}_{1-a}\text{Bi}_{1-b})\text{Tl}_x\text{Br}_6$	Single crystal	Cooling crystallization	[57]
$\text{Cs}_2\text{Ag}(\text{Bi}_{1-x}\text{M}_x)\text{Br}_6$ (M=In, Sb)	Single crystal	Melt crystallization	[58]
$\text{Cs}_2\text{AgBiI}_6$	Nanocrystal	Antisolvent recrystallization	[50, 51]
		Anion exchange	
$\text{Cs}_2\text{AgInCl}_6$	Single crystal	Cooling crystallization	[59–61]
	Powder	Precipitating from cold HCl solution	
Mn-doped $\text{Cs}_2\text{AgInCl}_6$	Microcrystal	Hot injection	[62]
$\text{Cs}_2\text{NaBiI}_6$	Microcrystal	Hydrothermal method	[64]
$\text{Cs}_2\text{SnI}_6$	Microcrystal	Hot injection	[74–76]
	Nanocrystal		
Bi-doped $\text{Cs}_2\text{SnCl}_6$	Single crystal	Cooling crystallization	[77]
$\text{Cs}_2\text{PdBr}_6$	Single crystal	Cooling crystallization	[78]
	Nanocrystal	Antisolvent recrystallization	[79]
	Nanocrystal	Anion exchange	[79]
$\text{A}_2\text{TiBr}_6$ (A=K, Rb, Cs)	Powder	Molten salt	[80]
$\text{Cs}_2\text{TiI}_x\text{Br}_{6-x}$ ( $x=0, 2, 4, 6$ )	Powder	Melt crystallization	[81]
$(\text{MA})_2\text{KBiCl}_6$	Powder	Evaporating HCl solution to dryness	[38]
$(\text{MA})_2\text{TlBiBr}_6$	Single crystal	Hydrothermal method	[82]
$(\text{MA})_2\text{AgBiBr}_6$	Powder	Evaporating HBr solution to dryness	[83]
$(\text{MA})_2\text{AgSbI}_6$	Powder	Melt crystallization	[84]
$(\text{MA})_2\text{AgBiI}_6$	Powder	Melt crystallization	[85]
$(\text{MA})_2\text{KGdCl}_6$	Powder	Evaporating HCl solution to dryness	[86]
$(\text{MA})_2\text{KYCl}_6$			
$(\text{MA})_2\text{AgInBr}_6$	Single crystal	MAPbBr <sub>3</sub> -induced crystallization	[87]
$(\text{MA})_2\text{SnI}_6$	Powder	Mixed iodides	[88]

in cubic  $\overline{\text{Fm}}3\text{m}$  symmetry and shows light absorption at the visible range of the spectrum [48, 49, 52]. Woodward et al. [48] measured diffuse reflectance to reveal bandgaps of 2.19 and 2.77 eV for  $\text{Cs}_2\text{AgBiBr}_6$  and  $\text{Cs}_2\text{AgBiCl}_6$ , respectively, as shown in Fig. 2a. The band structure calculation indicates that the interaction between Ag 4d orbitals and 3p/4p orbitals of the halide ions modifies valence band, leading to an indirect bandgap. Both compounds are stable when

exposed to air; however,  $\text{Cs}_2\text{AgBiBr}_6$  degrades over a period of weeks when exposed to ambient air and light. Meanwhile, Karunadasa et al. [52] tried to synthesize highly thermal and moisture-stable  $\text{Cs}_2\text{AgBiBr}_6$  single crystal with an indirect bandgap of 1.95 eV and photoluminescence (PL) lifetime of ~660 ns, as shown in Fig. 2b, which is very encouraging for photovoltaic applications. Then, Giustino et al. [49] designed and synthesized  $\text{Cs}_2\text{AgBiCl}_6$  with

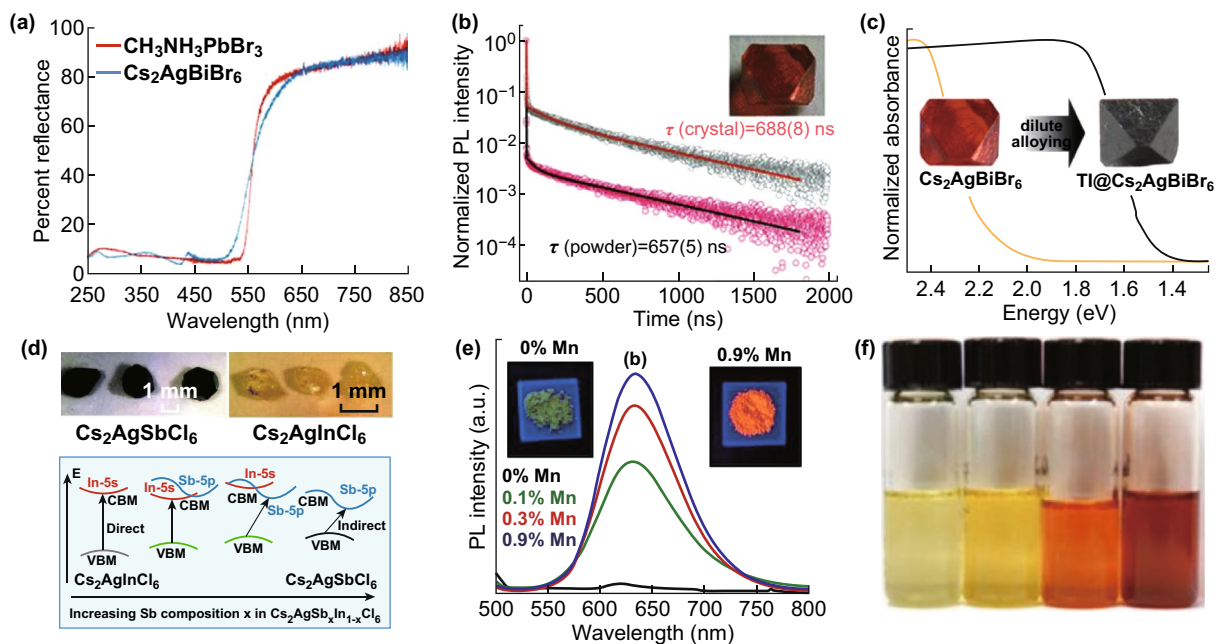


**Fig. 2** **a** Diffuse reflectance spectra of  $\text{Cs}_2\text{AgBiBr}_6$  and  $\text{CH}_3\text{NH}_3\text{PbBr}_3$ . Reproduced with permission from Ref. [48]. **b** Time-resolved room-temperature PL and fits for the PL decay time ( $\tau$ ) in powder and single-crystal samples. The inset is the photograph of a  $\text{Cs}_2\text{SgBiBr}_6$  single crystal. Reproduced with permission from Ref. [52]. **c** Apparent bandgaps of  $\text{Cs}_2\text{AgBiBr}_6$  and  $\text{Cs}_2(\text{Ag}_{1-a}\text{Bi}_{1-b})\text{Tl}_x\text{Br}_6$  ( $x = a + b = 0.075$ ) single crystals extracted by linear fits to  $\alpha^2$  vs.  $E$  (direct gap) and  $\alpha^{1/2}$  vs.  $E$  plots (indirect gap). Reproduced with permission from Ref. [57]. **d** Photographs of  $\text{Cs}_2\text{AgSbCl}_6$  and  $\text{Cs}_2\text{AgInCl}_6$  single crystals (top), and band diagram. A change in the character of the conduction band minimum (CBM) from s orbital derived to p orbital derived while having the valence band maximum (VBM) primarily Ag-d states results in a transition from direct to indirect bandgap. Reproduced with permission from Ref. [59]. **e** PL spectra of Mn-doped  $\text{Cs}_2\text{AgInCl}_6$  with different Mn contents, after excitation with 340 nm light. Insets show photographs of luminescence from powder samples under UV light. Reproduced with permission from Ref. [62]. **f** Photograph of dilute toluene solutions of  $\text{Cs}_2\text{AgBiBr}_6$ ,  $\text{Cs}_2\text{AgBiBr}_{5.2}\text{I}_{0.8}$ ,  $\text{Cs}_2\text{AgBiBr}_{1.6}\text{I}_{4.4}$  and  $\text{Cs}_2\text{AgBiI}_6$  nanocrystals. Reproduced with permission from Ref. [51]

bandgaps between 1.95 and 3.04 eV. However, the bandgap of  $\text{Cs}_2\text{AgBiX}_6$  ( $X = \text{Cl}, \text{Br}$ ) is indirect and slightly large, not ideal for thin-film photovoltaic applications. To engineer the bandgaps, Karunadasa et al. [52, 57] tried to incorporate Tl as a dilute impurity into their reported  $\text{Cs}_2\text{AgBiBr}_6$  single crystals. After incorporating Tl, the color changed to opaque black from translucent orange, which reflects the reduction of the bandgaps, as shown in Fig. 2c. The Tl content can be tuned across the series  $\text{Cs}_2(\text{Ag}_{1-a}\text{Bi}_{1-b})\text{Tl}_x\text{Br}_6$  ( $0.003 < x = a + b < 0.075$ ), and  $\text{Cs}_2(\text{Ag}_{1-a}\text{Bi}_{1-b})\text{Tl}_x\text{Br}_6$  ( $x = 0.075$ ) displays low indirect and direct bandgaps of 1.40 and 1.57 eV, respectively. Importantly, time-resolved photoconductivity measurements reveal long-lived carriers with microsecond lifetimes in the alloyed material, suggesting that carriers can be efficiently extracted in a solar cell [53]. The alloyed perovskite is the first halide double perovskite to show comparable bandgap and carrier lifetime to those of  $\text{CH}_3\text{NH}_3\text{PbI}_3$ , but unfortunately the content of Tl is still toxic [53, 57]. In 2017, Yan et al. [58] used  $\text{Cs}_2\text{AgBiBr}_6$  as

a host to engineer the bandgap through alloying of  $\text{In}^{3+}$  and  $\text{Sb}^{3+}$ .  $\text{Cs}_2\text{Ag}(\text{Bi}_{1-x}\text{M}_x)\text{Br}_6$  ( $M = \text{In}, \text{Sb}$ ) accommodates up to 75%  $\text{In}^{3+}$  with increased bandgap, and up to 37.5%  $\text{Sb}^{3+}$  with reduced bandgap, that is, enabling  $\sim 0.41$  eV bandgap modulation through introduction of the two metals, with smallest value of 1.86 eV for  $\text{Cs}_2\text{Ag}(\text{Bi}_{0.625}\text{Sb}_{0.375})\text{Br}_6$ . Band structure calculations indicate that opposite bandgap shift directions associated with Sb/In substitution arise from different atomic configurations for these atoms. Similarly, McQueen et al. [59] designed indirect and direct bandgap transitions using alloy strategy, as shown in Fig. 2d. The synthesized  $\text{Cs}_2\text{AgSbCl}_6$  and  $\text{Cs}_2\text{AgInCl}_6$  single crystals have indirect and direct bandgaps, respectively. When increasing Sb composition  $x$  in  $\text{Cs}_2\text{AgSb}_x\text{In}_{1-x}\text{Cl}_6$ , the compounds gradually transit from direct to indirect bandgap. Later on, Giustino et al. [60] identified that  $\text{Cs}_2\text{InAgCl}_6$  has direct bandgap of 3.3 eV and the compound is found to be photosensitive and turns reversibly from white to orange under ultraviolet (UV) illumination. Typically,  $\text{Cs}_2\text{InAgCl}_6$  exhibits a wide bandgap

which limits its application in the visible region. In 2018, Nag et al. [62] imparted the visible-light emission property in direct bandgap  $\text{Cs}_2\text{AgInCl}_6$  by doping  $\text{Mn}^{2+}$  ions, as shown in Fig. 2e.  $\text{Cs}_2\text{AgInCl}_6$  host absorbs UV light and then transfers the excitation energy to Mn d electrons. For X-site in perovskites, the Bohr radii gradually increase from F to I elements, resulting in increasing tightly bound nature and bandgaps [63]. Obviously, the X elements in the synthesized halide double perovskites are usually Cl or Br, and the bandgaps are relatively large. Gamelin et al. [51] synthesized  $\text{Cs}_2\text{AgBiX}_6$  (X=Cl, Br) colloidal nanocrystals by a hot-injection approach, which were converted to new materials including  $\text{Cs}_2\text{AgBiI}_6$  with a narrow bandgap about 1.75 eV through anion exchange. Figure 2f shows the photograph of dilute toluene solutions of (left to right)  $\text{Cs}_2\text{AgBiBr}_6$ ,  $\text{Cs}_2\text{AgBiBr}_{5.2}\text{I}_{0.8}$ ,  $\text{Cs}_2\text{AgBiBr}_{1.6}\text{I}_{4.4}$  and  $\text{Cs}_2\text{AgBiI}_6$  nanocrystals, and the dark red color of  $\text{Cs}_2\text{AgBiI}_6$  reflects that the absorption extends throughout the visible region. Recently, Ma et al. [64] reported first time the synthesis of novel halide double perovskite material of  $\text{Cs}_2\text{NaBiI}_6$  and determined its crystal structure by XRD and XPS tests and optical properties by UV-Vis absorption spectra.  $\text{Cs}_2\text{NaBiI}_6$  has a low direct bandgap of 1.66 eV and exhibits high stability against moisture and oxygen in ambient air.

To seek halide double perovskites theoretically, Zhang et al. [65–69] designed a series of all-inorganic halide double perovskites through first-principles calculations for the last 2 years. Photovoltaic-functionality-directed material screening process involves totally sixty-four candidate materials to identify 11 Sb- and Bi-based optimal materials containing intrinsic thermodynamic stability, suitable bandgaps, small carrier effective masses and low excitons binding energies as promising photovoltaic materials. When the monovalent ion is  $\text{Tl}^+$  or  $\text{In}^+$ , the materials have direct bandgap, among which  $\text{Cs}_2\text{InSbCl}_6$  and  $\text{Cs}_2\text{InBiCl}_6$  have the bandgap about 1.0 eV, and show the theoretical maximum performance comparable to that of  $\text{CH}_3\text{NH}_3\text{PbI}_3$ . However, the Tl is still toxic and the  $\text{In}^+$  is unstable by spontaneous oxidation into  $\text{In}^{3+}$  [70]. They simultaneously designed trivalent  $\text{In}^{3+}$  ion with monovalent  $\text{Ag}^+$  or  $\text{Cu}^+$  ion to find halide double perovskites [69]. Among them,  $\text{Rb}_2\text{CuInCl}_6$ ,  $\text{Rb}_2\text{AgInBr}_6$  and  $\text{Cs}_2\text{AgInBr}_6$  have direct bandgaps of 1.36, 1.46 and 1.50 eV, respectively, and theoretical spectroscopic limited maximal efficiency comparable to  $\text{CH}_3\text{NH}_3\text{PbI}_3$ .

It is noteworthy that there is another type of halide double perovskite as vacancy-ordered  $\text{A}_2\text{M(IV)X}_6$  (M(IV)=Sn,

Ti, Pd, Te, etc.), which not only proposes direct bandgaps, but also intrinsic stability and non-/low toxicity [71–73]. In 2014, Kanatzidis et al. [74] prepared  $\text{Cs}_2\text{SnI}_6$  microcrystal by a hot-injection method.  $\text{Cs}_2\text{SnI}_6$  nanocrystal was prepared with controlled shapes by the same method [75, 76]. The bandgap of the  $\text{Cs}_2\text{SnI}_6$  was found to be varied in the range of 1.36–1.67 eV. Quantum confinement effect has been observed for the nanoparticles of dimension below 8 nm. In 2018, Tang et al. [77] fabricated Bi-doped  $\text{Cs}_2\text{SnCl}_6$  single crystals, where the photoluminescence was observed from  $\text{Bi}^{3+}$  ions. In 2017, Snaith et al. [78] reported  $\text{Cs}_2\text{PdBr}_6$  single crystal, which exhibits long-lived photoluminescence, direct bandgap of 1.6 eV and long-term stability. In 2018, Kuang et al. [79] used antisolvent recrystallization method to prepare  $\text{Cs}_2\text{PdBr}_6$  nanocrystals with an average particle diameter of 2.8 nm. Such  $\text{Cs}_2\text{PdBr}_6$  nanocrystals not only display high stability against light illumination (one sun for more than 1000 h), moisture (70% for 2 months) and high temperature (120 °C for 600 h) conditions but also possess intriguing optical and ultrafast photophysical properties with a narrow direct bandgap of 1.69 eV. Further, a fast anion exchange method is adopted to prepare the  $\text{Cs}_2\text{PdI}_6$  nanocrystals. Another Ti-based vacancy-ordered halide double perovskites can start back in the early 1960s, and  $\text{K}_2\text{TiBr}_6$ ,  $\text{Rb}_2\text{TiBr}_6$  and  $\text{Cs}_2\text{TiBr}_6$  were prepared by using fused  $\text{SbBr}_3$  as the solvent [80]. However, the studies of them in optoelectronics have not been performed until 2018, and Zhou et al. [81] synthesized a series of  $\text{Cs}_2\text{TiI}_x\text{Br}_{6-x}$  ( $x=0, 2, 4, 6$ ) powers using the melt crystallization method, of which the bandgap can be tuned continuously from 1.02 to 1.78 eV. The present vacancy-ordered halide double perovskites possess several desirable properties, including ultra-stability, suitable direct bandgap, excellent optical absorption and benign defect.

## 2.2 Hybrid Halide Double Perovskites

To date, there have been synthesized nine hybrid halide double perovskites to the best of our knowledge, which are  $(\text{MA})_2\text{KBiCl}_6$  [38],  $(\text{MA})_2\text{TlBiBr}_6$  [82],  $(\text{MA})_2\text{AgBiBr}_6$  [83],  $(\text{MA})_2\text{AgSbI}_6$  [84],  $(\text{MA})_2\text{AgBiI}_6$  [85],  $(\text{MA})_2\text{KGdCl}_6$  [86],  $(\text{MA})_2\text{KYCl}_6$  [86],  $(\text{MA})_2\text{AgInBr}_6$  [87], and  $(\text{MA})_2\text{SnI}_6$  [88], as listed in Table 1. In 2016, the first hybrid halide double perovskite  $(\text{MA})_2\text{KBiCl}_6$  was synthesized by evaporating HCl solution to dryness [38]. In the Tauc plot from

the reflectance spectrum, there are two edges with values of 3.04 and 3.37 eV in Fig. 3a, in accordance with the theoretically calculated indirect bandgap of 3.02 eV and direct bandgap of 3.15 eV as shown in Fig. 3b, c. Further, density functional theory screening of  $(MA)_2MBiX_6$  ( $M=K, Cu, Ag, Tl$ ;  $X=Cl, Br, I$ ) shows that systems with bandgaps similar to those of the  $CH_3NH_3PbX_3$  lead compounds can be expected for  $M=Cu, Ag, Tl$ . Motivated by these findings,  $(MA)_2TlBiBr_6$ , isoelectronic with  $CH_3NH_3PbBr_3$ , was synthesized and found to have a direct bandgap of 2.16 eV, as shown in Fig. 3d [82]. However, despite its interesting electronic properties, the severe toxicity of Tl precludes  $(MA)_2TlBiBr_6$  from being a practical alternative to the Pb analog. Subsequently, they synthesized a hybrid halide double perovskite,  $(MA)_2AgBiBr_6$ , that has a low indirect bandgap of 2.02 eV and is relatively stable and nontoxic [83]. The material is stable in air and moisture and exhibits higher decomposition temperature than that of  $MAPbBr_3$ . In 2017, the same group synthesized  $(MA)_2AgSbI_6$  [84] and  $(MA)_2AgBiI_6$  [85] with indirect bandgap of  $\sim 2$  eV and exhibited high stability in air, as the XRD patterns shown in Fig. 3e, f. Though Sb and Bi are in the same group, there are still some differences between them. Compared with

Bi atom, Sb atom has a smaller mass and ion radius and the smaller ion radius of Sb leads to structural distortion of  $(MA)_2AgSbI_6$ , while the structure of  $(MA)_2AgBiI_6$  is the orthogonal phase. Besides, due to the seriously relativistic effects in heavy metal atom Bi, the impact of spin-orbit coupling on bandgap of  $(MA)_2AgBiI_6$  is more pronounced. Simultaneously,  $(MA)_2KAgCl_6$  and  $(MA)_2KYCl_6$  have been synthesized by a solution evaporation method, which adopt a rhombohedral structure with  $R\bar{3}m$  symmetry [86]. Both phases exhibit a rhombohedral-to-cubic phase transition on heating to  $\sim 435$  K as shown in Fig. 3g. Density functional calculations on the rhombohedral phase indicate that both materials have large direct bandgaps about 5 eV and mechanical stability. In 2018,  $(MA)_2AgInBr_6$  single crystal [87], as shown in Fig. 3h, is obtained through the use of  $Pb^{2+}$  (from  $CH_3NH_3PbBr_3$ ) to modulate the soluble intermediates and force the formation. In the same year,  $(MA)_2SnI_6$  powder was obtained by mixing  $SnI_4$  with  $CH_3NH_3I$  powder at room temperature [88]. The powder was evaporated in a tungsten boat at  $120^\circ C$  in a vacuum chamber to deposit the  $(MA)_2SnI_6$  films. The films have a direct bandgap of 1.81 eV with a strong absorption coefficient of  $\sim 7 \times 10^4$   $cm^{-1}$ . In addition, the films were n type with a carrier concentration

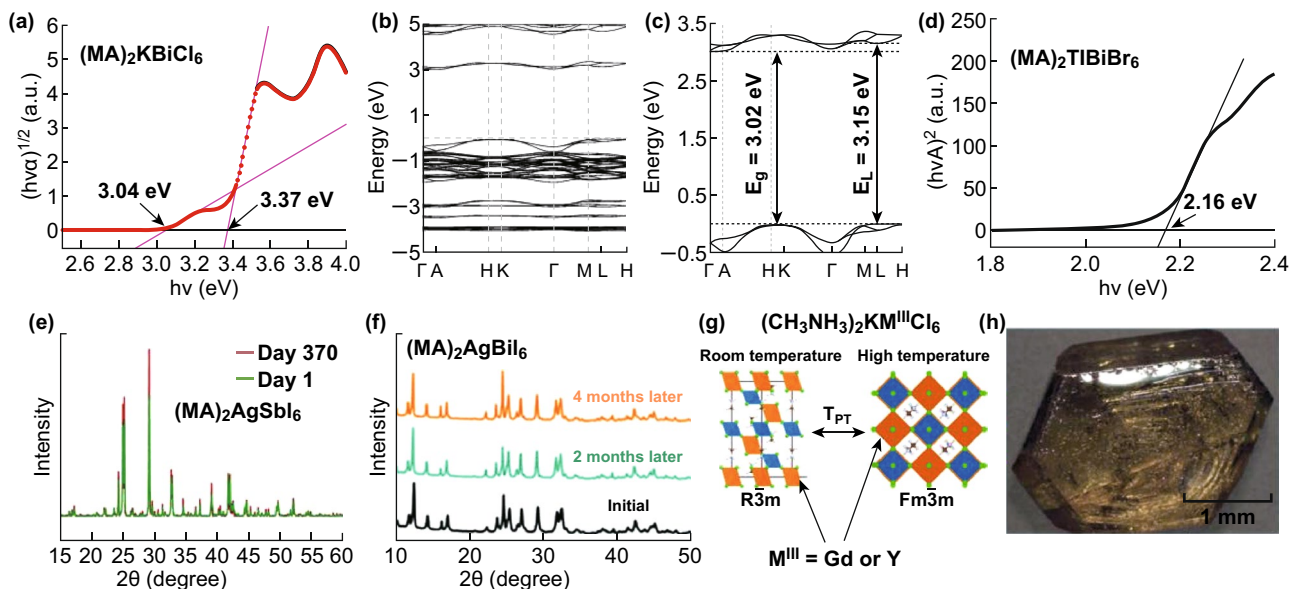


**Fig. 3** **a** Tauc plot (assumed indirect bandgap), **b-c** calculated band structure of  $(MA)_2KBiCl_6$  and the enlarged view of the band structure near the bandgap. Reproduced with permission from Ref. [38]. **d** Tauc plot (assumed direct bandgap) of  $(MA)_2TlBiBr_6$ . Reproduced with permission from Ref. [82]. **e** XRD patterns of fresh  $(MA)_2AgSbI_6$  compared to  $(MA)_2AgSbI_6$  after 370 days of exposure to air. Reproduced with permission from Ref. [84]. **f** Air stability of  $(MA)_2AgBiI_6$ . Reproduced with permission from Ref. [85]. **g** Schematic illustration of rhombohedral-to-cubic phase transition on high-temperature heating for  $(MA)_2KAgCl_6$  and  $(MA)_2KYCl_6$ . Reproduced with permission from Ref [86]. **h** Photograph of a  $(MA)_2AgBiBr_6$  single crystal. Reproduced with permission from Ref. [87]

of  $\sim 2 \times 10^{15} \text{ cm}^{-3}$  and an electron mobility of  $\sim 3 \text{ cm}^2/\text{V}\cdot\text{s}$ . Moreover, the conductivity was increased by a factor of 4 under simulated solar illumination ( $100 \text{ mW cm}^{-2}$ ). These results indicate that  $(\text{MA})_2\text{SnI}_6$  is a lead-free optical semiconductor suitable for solar cell applications. The synthesized hybrid halide double perovskites indicate substantially better stability, unlike  $\text{CH}_3\text{NH}_3\text{PbI}_3$ . However, to the best of our knowledge, there are no reports about applications of hybrid halide double perovskites.

### 3 Optoelectronic Applications

#### 3.1 Photodetectors

In 2017, Tang et al. [61] successfully prepared high-quality  $\text{Cs}_2\text{AgInCl}_6$  single crystals with a low trap state density ( $(8.6 \pm 1.9) \times 10^8 \text{ cm}^{-3}$ ) by a hydrothermal method, which were further applied in UV detectors. The obtained results experimentally verified the existence of parity-forbidden transition [89] and identified that the oxygen was effective on the optical properties. By eliminating oxygen contamination in vacuum,  $\text{Cs}_2\text{AgInCl}_6$  single crystal-based UV detector showed best performance with visible blind, high ON–OFF ratio ( $\sim 500$ ), fast photoresponse ( $\sim 1 \text{ ms}$ ), low dark current ( $\sim 10 \text{ pA}$  at  $5 \text{ V}$  bias) and high detectivity ( $\sim 1012 \text{ Jones}$ ). If the Cl is replaced by Br in  $\text{Cs}_2\text{AgInX}_6$  compounds, the bandgaps reduce and absorption range can be extended to visible region. Shi et al. [90] used a one-step spin-coating method to prepare  $\text{Cs}_2\text{AgBiBr}_6$  thin films for photodetectors. The device exhibits high responsivity of  $7.01 \text{ A W}^{-1}$ , ON–OFF ratio of  $2.16 \times 10^4$ , specific detectivity of  $5.66 \times 10^{11} \text{ Jones}$ , EQE of 2146% and demonstrates remarkable stability against the water and oxygen degradation. Wang et al. [91] fabricated highly efficient and stable self-powered UV and deep-blue detector based on  $\text{Cs}_2\text{AgBiBr}_6/\text{SnO}_2$  heterojunction, as shown in Fig. 4a. The photogenerated carriers in  $\text{Cs}_2\text{AgBiBr}_6$  film can be separated at the  $\text{Cs}_2\text{AgBiBr}_6/\text{SnO}_2$  heterojunction interface by its built-in field, as illustrated in Fig. 4b. The device is self-powered with two responsivity peaks at 350 and 435 nm, which is suitable for UV (320–400 nm) and deep-blue light detection, as shown in Fig. 4c. A high responsivity of  $0.11 \text{ A W}^{-1}$  at 350 nm and a quick response time of less than 3 ms are obtained, which are significantly higher than those of other semiconductor oxide heterojunction-based UV detectors.

More importantly, the photocurrent shows no noticeable degradation after more than 6 months of storage in ambient conditions without encapsulation, as shown in Fig. 4d. In addition, the aforementioned vacancy-ordered double perovskites of  $\text{Cs}_2\text{PdBr}_6$  single crystal and  $\text{Cs}_2\text{SnI}_6$  nanocrystal were successfully applied in stable and fast photodetectors [75, 78]. Consequently, the halide double perovskite-based photodetectors displayed high efficiency and stability and environmental friendliness, which are potential alternatives for practical applications.

#### 3.2 X-ray Detectors

In 2017, Tang et al. [54] also prepared  $\text{Cs}_2\text{AgBiBr}_6$  single crystals by controlling cooling rate in a solution for sensitive X-ray detectors with a low detection limit. The  $\text{Cs}_2\text{AgBiBr}_6$  single crystals can directly convert X-rays into electrical signals due to the high average atomic number, high carrier drift length per unit electric field, low ionization energy and high resistivity. The optimized device exhibited high sensitivity of  $105 \mu\text{C}/\text{Gyair}/\text{cm}^2$ , low detection limit of  $59.7 \text{ nGyair s}^{-1}$  under an external bias of  $5 \text{ V}$  and demonstrated long-term operational stability, as shown in Fig. 5a, b, all of which are crucial for potential applications in X-ray security screening systems and medical diagnostics. Subsequently, Yu et al. [92] used composite films of  $\text{Cs}_2\text{AgBiBr}_6$  embedded in a polymer matrix for X-ray detectors. The polymer with hydroxyl functional groups can greatly improve the uniformity of the composite films, and large area dense films can be obtained by a simple drop-casting process. X-ray detectors based on the composite films exhibit a sensitivity of  $40 \mu\text{C}/\text{Gyair}/\text{cm}^2$  under an external bias of  $400 \text{ V}$ , as shown in Fig. 5c, and tolerate a 5% tensile/compressive strain in the composite films without performance degradation. Pixelated X-ray detectors fabricated on the same composite film can realize X-ray imaging and resolve a proof-of-concept geometric pattern. Recently, Tang et al. [93] have used lanthanide series as trivalent metals to obtain highly stable halide double perovskites ( $\text{Cs}_2\text{NaLnCl}_6$ , Ln=Tb or Eu) with high scintillation light yield. The crystals exhibit typical f–f transitions of lanthanide cations, while  $\text{Cs}_2\text{NaTbCl}_6$  exhibits strong green photoluminescence and  $\text{Cs}_2\text{NaEuCl}_6$  exhibits red photoluminescence. Under X-ray radiations, the light yield of  $\text{Cs}_2\text{NaTbCl}_6$  reaches  $46,600 \text{ photons MeV}^{-1}$ , much higher than that of the commercially used  $(\text{Lu}, \text{Y})_2\text{SiO}_5:\text{Ce}^{3+}$

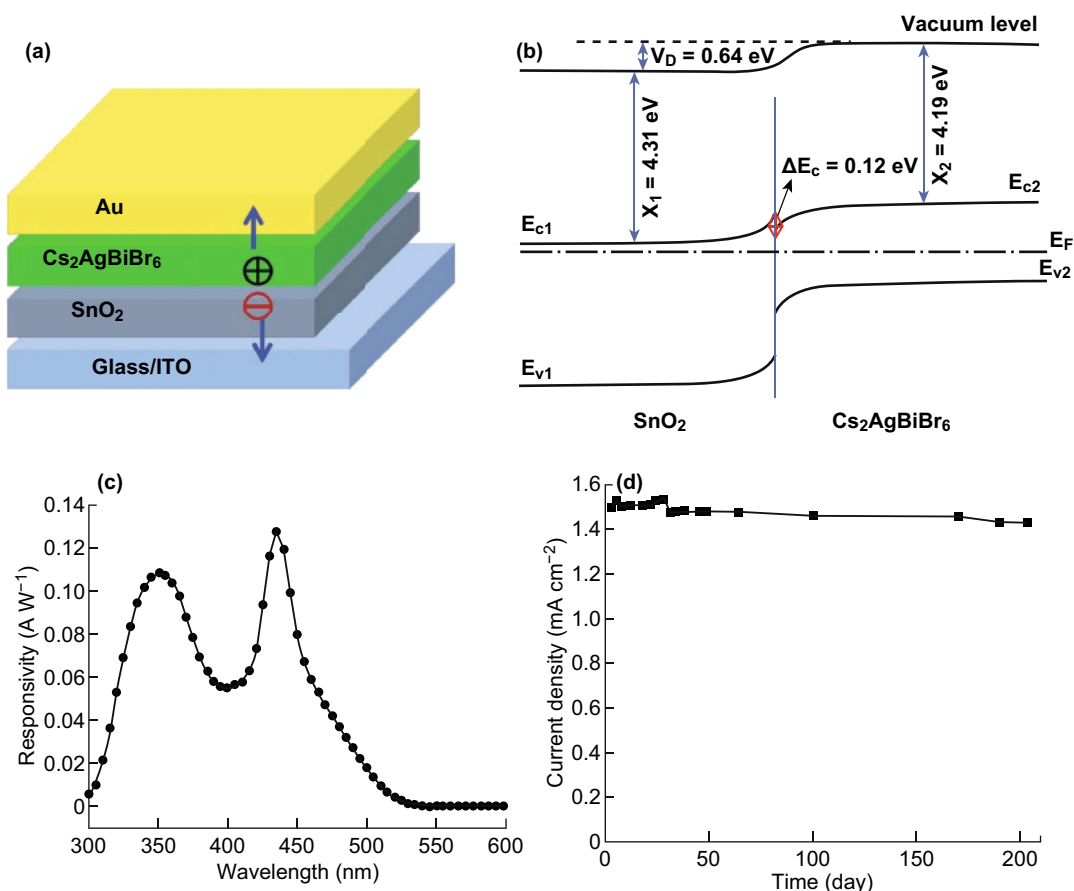


**Fig. 4** **a** Configuration diagram of  $\text{Cs}_2\text{AgBiBr}_6$ -based photodetector. **b** Band scheme diagram of  $\text{Cs}_2\text{AgBiBr}_6/\text{SnO}_2$  heterojunction. **c** Responsivity of photodetector at zero bias. **d** Long-term stability test of  $\text{Cs}_2\text{AgBiBr}_6$ -based photodetector. Reproduced with permission from Ref. [91]

crystals (LYSO, 28,500 photons  $\text{MeV}^{-1}$ ), as shown in Fig. 5d. Lanthanide-based halide double perovskites open up a new route toward radiation detections and potential medical imaging.

### 3.3 Photocatalyst

In 2018, Kuang et al. [56] fabricated  $\text{Cs}_2\text{AgBiBr}_6$  nanocrystals (NCs) via a simple hot-injection method for photocatalytic  $\text{CO}_2$  reduction. The  $\text{Cs}_2\text{AgBiBr}_6$  NCs can maintain their structure stability in low-polarity solutions (up to 3 weeks) and phase uniformity against 55% relative humidity for 90 days, light-soaking stability toward  $70 \text{ mW cm}^{-2}$  for 500 h or  $100^\circ\text{C}$  heating for 300 h, thus declaring the impressive stability in moisture, light and temperature. Photocatalytic  $\text{CO}_2$  was conducted in ethyl acetate in a Pyrex glass bottle under simulated solar light (AM 1.5G,  $150 \text{ mW cm}^{-2}$ ) illumination. After the constant irradiation for 6 h, the

pristine  $\text{Cs}_2\text{AgBiBr}_6$  NCs could afford the evolution of CO and  $\text{CH}_4$  with 5.5 and  $0.65 \mu\text{mol g}^{-1}$ , respectively. Meanwhile, the electron consumption attained  $16.2 \mu\text{mol g}^{-1}$ , as shown in Fig. 6a. On the contrary, the washed  $\text{Cs}_2\text{AgBiBr}_6$  NCs have boosted the evolution of R(CO) and R( $\text{CH}_4$ ) to 14.1 and  $9.6 \mu\text{mol g}^{-1}$ , presenting a 6.5-fold enhancement in the electron consumption. A tentative mechanism for the photocatalytic  $\text{CO}_2$  reduction over the  $\text{Cs}_2\text{AgBiBr}_6$  NCs is proposed in Fig. 6b, in which the  $\text{Cs}_2\text{AgBiBr}_6$  NCs have a suitable conduction band to drive  $\text{CO}_2$  reduction. The time-dependent evolution of CO and  $\text{CH}_4$  using the as-prepared and -washed NCs by absolute ethanol as photocatalysts under light irradiation is shown in Fig. 6c, where the evolution of CO and  $\text{CH}_4$  rose nearly linearly with irradiation time and the washed NCs exhibited higher efficiency for  $\text{CO}_2$  conversion. Therefore, the novel  $\text{Cs}_2\text{AgBiBr}_6$  NCs were successfully used to conduct the  $\text{CO}_2$  reduction reactions with

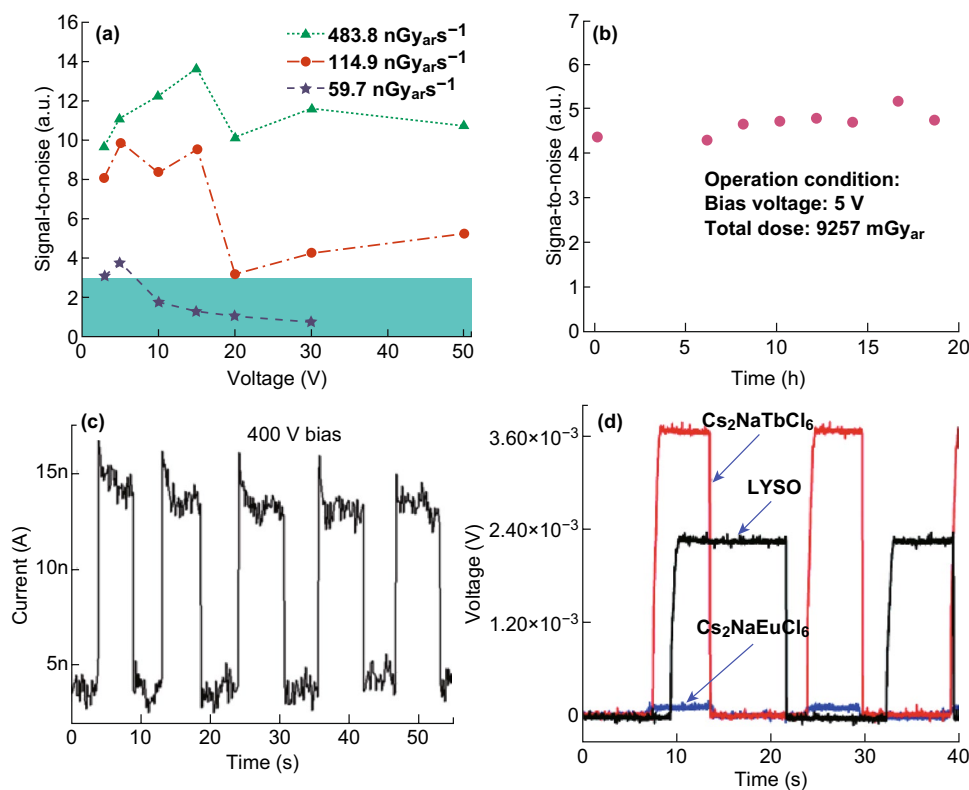


**Fig. 5** **a** Signal-to-noise ratio of the device derived by calculating the standard deviation of the X-ray photocurrent. The red dashed line represents a SNR of 3, and thus the detection limit is 59.7 nGy<sub>ar</sub> s<sup>-1</sup> at 5 V bias, as indicated by the purple star surrounded by the red dashed circle. **b** Operational stability of our Cs<sub>2</sub>AgBiBr<sub>6</sub> single-crystal X-ray detector. Testing conditions: continued 138.7 μGy<sub>air</sub> s<sup>-1</sup> X-ray irradiation with constant 5 V bias, tested in ambient air without any encapsulation. Reproduced with permission from Ref. [54]. **c** Transient responses of the detector at a constant 400 V. Reproduced with permission [92]. **d** The generated voltage of multiplier tubes by scintillation light of Cs<sub>2</sub>NaTbCl<sub>6</sub> (red line), Cs<sub>2</sub>NaEuCl<sub>6</sub> (blue line) and (Lu,Y)<sub>2</sub>SiO<sub>5</sub>:Ce<sup>3+</sup> (LYSO, black line), respectively (color online). Reproduced with permission from Ref. [93]. (Color figure online)

high selectivity and stability, which hold great potential in the further photochemical applications.

### 3.4 LEDs

Tang et al. [77] used the synthesized Bi-doped Cs<sub>2</sub>SnCl<sub>6</sub> as blue emissive phosphors, where Bi<sup>3+</sup> is the luminescent dopant. Hybrid density functional theory calculations suggest the preferred formation of [Bi<sub>Sn</sub> + V<sub>Cl</sub>] defect complex, responsible for the optical absorption and the associated blue emission. The Bi-doped Cs<sub>2</sub>SnCl<sub>6</sub> also shows impressive thermal and water stability due to its inorganic nature and the formation of protective BiOCl layer. A significant boost of the photoluminescence (emission peak: 455 nm, PLQY: 78.9%) was observed upon doping. This is the highest PLQY ever reported for all-inorganic lead-free perovskites and even comparable to the highest value of lead perovskites with

blue emissions. Bi-doped Cs<sub>2</sub>SnCl<sub>6</sub> showed great potential as blue phosphors, and its LED exhibited a warm white high light emission with a correlated color temperature of 4486 K and a Commission Internationale de l'Éclairage coordinate of (0.36; 0.37) when integrated with yellow phosphor. Recently, Tang et al. [94] broke the parity-forbidden transition of Cs<sub>2</sub>AgInCl<sub>6</sub> by alloying Na<sup>+</sup> cations, which leads to efficient white emission via radiative recombination of self-trapped excitons. The Bi<sup>3+</sup> incorporation is believed to improve crystal perfection and promote exciton localization [95]. The optimally alloyed Cs<sub>2</sub>(Ag<sub>0.60</sub>Na<sub>0.40</sub>)InCl<sub>6</sub> with 0.04% Bi<sup>3+</sup> doping emits warm white light with (86 ± 5) % quantum efficiency and works for over 1000 h. Therefore, halide double perovskites hold great potential for display and lighting applications and merit further study to realize their full potential.

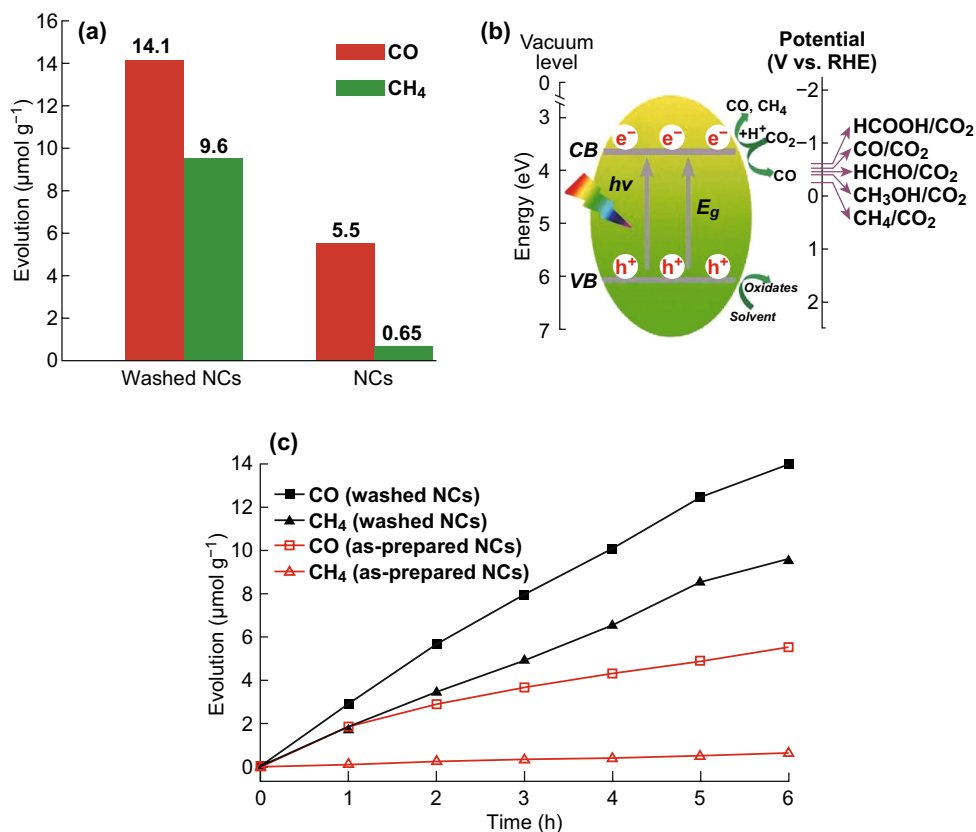


**Fig. 6** **a** Comparison of photocatalytic CO<sub>2</sub> reduction performance of the as-prepared Cs<sub>2</sub>AgBiBr<sub>6</sub> NCs and washed NCs. **b** Schematic diagram of the photoreduction of CO<sub>2</sub> on the surface of Cs<sub>2</sub>AgBiBr<sub>6</sub> NCs. **c** Time course of CO and CH<sub>4</sub> evolutions over as-prepared and -washed Cs<sub>2</sub>AgBiBr<sub>6</sub> NCs. Reproduced with permission from Ref. [56]

### 3.5 Solar Cells

To date, Cs<sub>2</sub>AgBiBr<sub>6</sub> is most applied in halide double perovskite-based solar cells [96–100]. In 2017, Bein et al. [96] fabricated Cs<sub>2</sub>AgBiBr<sub>6</sub> films by a spin-coating method and incorporated them into solar cells for the first time. After optimized synthesis conditions, the Cs<sub>2</sub>AgBiBr<sub>6</sub>-based solar cells revealed power conversion efficiency (PCE) of 2.43% and excellent stability upon exposure without encapsulation. Inadequately, there is a thick agglomerated morphology of the Cs<sub>2</sub>AgBiBr<sub>6</sub> films with micrometer-sized grains on the surface, and the hysteresis of the devices is serious. In 2018, Wang et al. [97] developed planar heterojunction solar cells with high-quality Cs<sub>2</sub>AgBiBr<sub>6</sub> film by low-pressure-assisted solution processing under ambient conditions, as shown in Fig. 7a, b, borrowing Cs<sub>2</sub>AgBiBr<sub>6</sub>/SnO<sub>2</sub> heterojunction from their reported detectors [91]. Orange Cs<sub>2</sub>AgBiBr<sub>6</sub> powder was dissolved in DMSO solution to form a light yellow transparent solution and then fabricate the film using spin-coating

technique, as presented in Fig. 7a. The spin-coated film was quickly moved to a low-pressure chamber pumped to 20 Pa, in which the transparent film would gradually turn to light yellow, as shown in Fig. 7b. Next, the as-prepared film was annealed and attained smooth morphology as shown in Fig. 7d. The optimized Cs<sub>2</sub>AgBiBr<sub>6</sub> film achieved 1.44% PCE of the solar cells with P3HT hole conductor layer. On the contrary, the traditional thermal annealing method generated rough Cs<sub>2</sub>AgBiBr<sub>6</sub> film in Fig. 7c, and the corresponding devices usually showed a poor PCE (<0.1%). Furthermore, these devices also showed hysteresis phenomenon. Wu et al. [98] used anti-solvent dropping technology and post-annealing process to realize high-quality Cs<sub>2</sub>AgBiBr<sub>6</sub> film with ultra-smooth morphology, microsized grains and high crystallinity (shown in Fig. 7e), which was applied in inverted planar heterojunction solar cells. The device shows PCE up to 2.23% with free hysteresis. Subsequently, Grancini et al. [99] realized hysteresis-free mesoporous double-perovskite solar cells by fine-tuning the material deposition

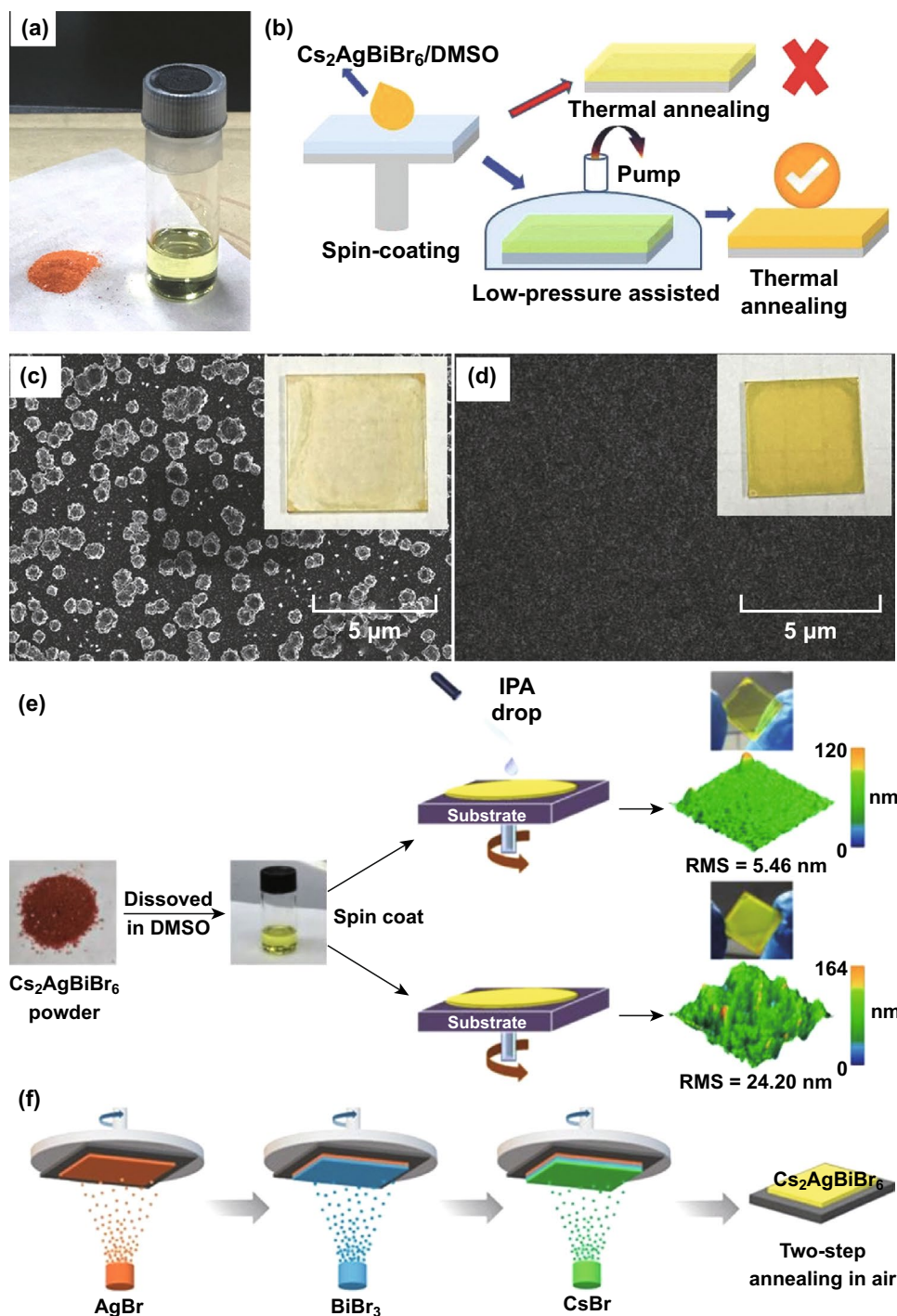


**Fig. 7** **a** Image of  $\text{Cs}_2\text{AgBiBr}_6$  powder (left) and solution in DMSO (right). **b** The film fabrication process diagram. **c**, **d** SEM images of film obtained by traditional thermally annealed and low-pressure-assisted process, respectively, inset: film photograph, size,  $25 \times 25 \text{ mm}^2$ . Reproduced with permission from Ref. [97]. **e** Schematic illustration of the spin-coating process with and without anti-solvent dropping protocol; the morphology of the as-prepared film can be improved after IPA dropping. Reproduced with permission from Ref. [98]. **f** Scheme of sequential vapor deposition processing of  $\text{Cs}_2\text{AgBiBr}_6$  double perovskite. Reproduced with permission from Ref. [100]

parameters, enabling the growth of a highly uniform and compact  $\text{Cs}_2\text{AgBiBr}_6$  film, and by engineering the device interfaces by screening different molecular and polymeric hole-transporting materials. Chlorobenzene was the anti-solution in the film formation before the annealing step. Recently, Liu et al. [100] utilized a sequential vapor deposition method to fabricate  $\text{Cs}_2\text{AgBiBr}_6$  films for solar cells, as shown in Fig. 7f. The two-step annealing process produces films with better quality in terms of crystallization and film uniformity. The solar cells with planar device structure show an optimized PCE of 1.37%, which can be maintained at 90% after 240 h of storage under ambient condition. In addition, Ma et al. [64] incorporated their synthesized  $\text{Cs}_2\text{NaBiI}_6$  into solar cells, which shows great stability and reproducibility.

It is greatly significant that the vacancy-ordered  $\text{A}_2\text{M(IV)X}_6$  halide double perovskites have direct suitable bandgaps, which have been successfully applied in solar cells [74, 101–104]. In 2014, Kanatzidis et al. [74] first time introduced  $\text{Cs}_2\text{SnI}_6$  as a hole-transporting material in dye-sensitized solar cells. In 2016, Cao et al. [101] discovered that  $\text{B-}\gamma\text{-CsSnI}_3$  film can spontaneously convert to an air-stable  $\text{Cs}_2\text{SnI}_6$  film in air and at room temperature, which can be adopted as lead-free solar cell light absorber owing to its direct bandgap of 1.48 eV and high absorption coefficient (over  $105\text{ cm}^{-1}$  from 1.7 eV). A planar PSC using the  $\text{Cs}_2\text{SnI}_6$  film as the light absorber achieved PCE nearly 1% in air. Later on, Cao et al. [102] synthesized  $\text{Cs}_2\text{SnI}_6$  powder through a modified solution process and demonstrated its application as absorbing layer in mesoporous solar cell with a configuration of FTO/ZnO compact layer/nanorods/ $\text{Cs}_2\text{SnI}_6/\text{P}_3\text{HT}/\text{Ag}$ . With careful control of ZnO nanorod length and pore size to ensure high loading of the  $\text{Cs}_2\text{SnI}_6$  absorber, the PCE achieved was nearly 1%. The bandgap tuning achieved by substitution of Br is anticipated to enhance the open-circuit voltage of  $\text{Cs}_2\text{SnI}_6$ -based solar cell. The compounds are  $\text{Cs}_2\text{SnI}_{6-x}\text{Br}_x$  for a range of  $x$  that provide the desired bandgaps from 1.3 to 2.9 eV with  $x < 3$  being suitable for solar cell design. The cells show a PCE of 2.1% for the case of the  $x = 2$  compound [103]. Recently,  $\text{Cs}_2\text{TiBr}_6$  thin films were prepared through a facile low-temperature vapor-based method and incorporated into planar heterojunction PSCs [104]. The  $\text{Cs}_2\text{TiBr}_6$  thin films exhibit favorable bandgap of 1.8 eV, long and balanced carrier diffusion lengths, suitable energy levels and superior intrinsic and environmental stability, which result in a stable solar cell with efficiency up to 3.3%.

## 4 Conclusion and Perspective

Herein, we intend to summarize the most recent developments regarding halide double perovskite materials and the related applications. Due to distinguished stability and tunable properties, halide double perovskites have enormous potential leading to high-performance, stable and environmentally friendly optoelectronic devices for practical applications. Although significant progress has been achieved in halide double perovskites, there are still many challenges to be addressed.

Multitude of halide double perovskite materials to be existed is theoretically predicted, but a very limited number have been explored experimentally. In addition, synthesized strategies to those materials remain limited, which are mainly divided into solid-state and wet-chemical routes. The solid-state route is processed to heat anhydrous haloids as melt crystallization. Wet-chemical route includes hot injection, antisolvent recrystallization, hydrothermal methods, etc. The single crystals are classically obtained by the hydrothermal method through controlling the cooling rate from hot solution. Because a few iodine-based double perovskite materials are not easily obtained by direct combination of reactants, anion exchange and induced crystallization have been taken [51, 87]. Accordingly, we propose two aspects to make efforts: borrowing the present routes to explore the theoretical predictions and discovering viable routes to more halide double perovskite materials.

The present halide double perovskite materials exhibit excellent stability in moisture, heat and light, unlike the fashionable Pb-based perovskite materials. For instance,  $(\text{MA})_2\text{AgSbI}_6$  powder is relatively unaltered after being exposed to air for 370 days and the thermal stability can be up to 260 °C [84]. As a general rule, all-inorganic halide perovskites possess better stability [105–107].  $\text{Cs}_2\text{AgBiBr}_6$  single crystal is stable up to 430 °C, and differential thermal analysis indicates no phase transitions within this temperature range [42].  $\text{Cs}_2\text{NaBiI}_6$  exhibits superior stability against the moisture and the oxygen in the ambient air, which can be washed with water [53]. However, there is lack of proven stability under complicated environmental conditions or with long term over 10 years. In addition, the underlying cause of stability under different conditions remains covered. Hence, more attempts need to place emphasis on enhancing

long-term and complicated environmental stability, as well as discovering the stability mechanisms.

Hitherto, extremely few all-inorganic and no hybrid halide double perovskite materials have been developed for optoelectronic applications. More halide double perovskite materials are desirable to be developed and widely applied. Moreover, the optoelectronic devices based on single-crystal halide double perovskite materials enjoy pleasurable performance, comparable to that of Pb-based perovskite analogs, such as  $\text{Cs}_2\text{AgBiBr}_6$  single-crystal X-ray detectors [54]. However, the device performance of halide double perovskite films is still lower than that of the Pb-based perovskite analogs. The underlying causes can be ascribed to the underdeveloped electronic structures, material properties, film qualities of halide double perovskite materials and device architectures. It is difficult to develop a synthetic route to obtain uniform thin films of the correct phase and composition. Typically,  $\text{Cs}_2\text{AgBiBr}_6$  [96],  $\text{Cs}_2\text{SnI}_{6-x}\text{Br}_x$  [103] and  $\text{Cs}_2\text{TiBr}_6$  [104] absorbers in PSCs have achieved optimized efficiency of 2.4, 2.1 and 3.3%, respectively, far below that of the Pb-based perovskite analogs. To enhance  $\text{Cs}_2\text{AgBiBr}_6$ -film quality, anti-solvent dropping and low-pressure-assisted solution methods have been adopted [97, 98]. Interface engineering of device architectures was taken to achieve hysteresis-free  $\text{Cs}_2\text{AgBiBr}_6$ -based PSCs [99]. However, the performance is still unsatisfactory because  $\text{Cs}_2\text{AgBiBr}_6$  has a relatively large indirect bandgap. Various strategies can be attempted to engineer the bandgap and modify the device structures to improve the device performance, such as chemical doping and alloying approaches. Meanwhile, chemical doping and alloying approaches are expected to bring original effects for applications. As an example, Bi-doped  $\text{Cs}_2\text{SnCl}_6$  can be applied as blue emissive phosphors, where  $\text{Bi}^{3+}$  is the luminescent dopant [77].

In summary, we are very much optimistic that the current astonishing achievements will encourage more researchers to overcome the above challenges in the future.

**Acknowledgements** This work was financially supported by the Ministry of Education of China (IRT1148), the National Natural Science Foundation of China (U1732126, 11804166, 51602161, 51372119), the National Synergetic Innovation Center for Advanced Materials (SICAM), the China Postdoctoral Science Foundation (2018M630587), the Priority Academic Program Development of Jiangsu Higher Education Institutions (YX03001) and the Natural Science Foundation of NJUPT (NY217091).

**Open Access** This article is distributed under the terms of the Creative Commons Attribution 4.0 International License (<http://creativecommons.org/licenses/by/4.0/>), which permits unrestricted use, distribution, and reproduction in any medium, provided you give appropriate credit to the original author(s) and the source, provide a link to the Creative Commons license, and indicate if changes were made.

## References

1. A. Kojima, K. Teshima, Y. Shirai, T. Miyasaka, Organometal halide perovskites as visible-light sensitizers for photovoltaic cells. *J. Am. Chem. Soc.* **131**(17), 6050–6051 (2009). <https://doi.org/10.1021/ja809598r>
2. H.S. Kim, C.R. Lee, J.H. Im, K.B. Lee, T. Moehl et al., Lead iodide perovskite sensitized all-solid-state submicron thin film mesoscopic solar cell with efficiency exceeding 9%. *Sci. Rep.* **2**, 6022–6025 (2012). <https://doi.org/10.1038/srep00591>
3. H. Zhou, Q. Chen, G. Li, S. Luo, T.B. Song et al., Interface engineering of highly efficient perovskite solar cells. *Science* **345**(6196), 542–546 (2014). <https://doi.org/10.1126/science.1254050>
4. N.J. Jeon, J.H. Noh, W.S. Yang, Y.C. Kim, S. Ryu, J. Seo, S.I. Seok, Compositional engineering of perovskite materials for high-performance solar cells. *Nature* **517**, 476–480 (2015). <https://doi.org/10.1038/nature14133>
5. D. Luo, W. Yang, Z. Wang, A. Sadhanala, Q. Hu et al., Enhanced photovoltage for inverted planar heterojunction perovskite solar cells. *Science* **360**(6396), 1442 (2018). <https://doi.org/10.1126/science.aap9282>
6. National Renewable Energy Laboratory (NREL) (2018). <https://www.nrel.gov/pv/assets/pdfs/pv-efficiencies-chart.20181214.pdf>
7. M.M. Lee, J. Teuscher, T. Miyasaka, T.N. Murakami, H.J. Snaith, Efficient hybrid solar cells based on meso-structured organometal halide perovskites. *Science* **338**(6107), 643–647 (2012). <https://doi.org/10.1126/science.1228604>
8. S.D. Stranks, G.E. Eperon, G. Grancini, C. Menelaou, M.J.P. Alcocer, T. Leijtens, L.M. Hertz, A. Petrozza, H.J. Snaith, Electron-hole diffusion lengths exceeding 1 micrometer in an organometal trihalide perovskite absorber. *Science* **342**(6156), 341–344 (2013). <https://doi.org/10.1126/science.1243982>
9. G.C. Xing, N. Mathews, S.Y. Sun, S.S. Lim, Y.M. Lam, M. Gratzel, S. Mhaisalkar, T.C. Sum, Long-range balanced electron- and hole-transport lengths in organic-inorganic  $\text{CH}_3\text{NH}_3\text{PbI}_3$ . *Science* **342**(6156), 344–347 (2013). <https://doi.org/10.1126/science.1243167>
10. W.S. Yang, B.W. Park, E.H. Jung, N.J. Jeon, Y.C. Kim et al., Iodide management in formamidinium-lead-halide-based perovskite layers for efficient solar cells. *Science* **356**(6345), 1376–1379 (2017). <https://doi.org/10.1126/science.aan2301>
11. S.D. Stranks, H.J. Snaith, Metal-halide perovskites for photovoltaic and light-emitting devices. *Nat. Nanotech.* **10**(5), 391–402 (2015). <https://doi.org/10.1038/nnano.2015.90>

12. H. Cho, S.H. Jeong, M.H. Park, Y.H. Kim, C. Wolf, C.L. Lee et al., Overcoming the electroluminescence efficiency limitations of perovskite light-emitting diodes. *Science* **350**(6265), 1222–1225 (2015). <https://doi.org/10.1126/science.aad1818>
13. H. Zhu, Y. Fu, F. Meng, X. Wu, Z. Gong et al., Lead halide perovskite nanowire lasers with low lasing thresholds and high quality factors. *Nat. Mater.* **14**(6), 636–642 (2015). <https://doi.org/10.1038/nmat4271>
14. F. Zhang, B. Yang, K. Zheng, S. Yang, Y. Li, W. Deng, R. He, Formamidinium lead bromide (FAPbBr<sub>3</sub>) perovskite microcrystals for sensitive and fast photodetectors. *Nano-Micro Lett.* **10**(3), 43 (2018). <https://doi.org/10.1007/s40820-018-0196-2>
15. L. Chu, R. Hu, W. Liu, Y. Ma, R. Zhang, J. Yang, X. Li, Screen printing large-area organometal halide perovskite thin films for efficient photodetectors. *Mater. Res. Bull.* **98**, 322 (2018). <https://doi.org/10.1016/j.materresbull.2017.10.039>
16. Q. Chen, J. Wu, X. Ou, B. Huang, J. Almutlaq et al., All-inorganic perovskite nanocrystal scintillators. *Nature* **561**(7721), 88 (2018). <https://doi.org/10.1038/s41586-018-0451-1>
17. H. Luo, X. Lin, X. Hou, L. Pan, S. Huang, X. Chen, Efficient and air-stable planar perovskite solar cells formed on graphene-oxide-modified PEDOT:PSS hole transport layer. *Nano-Micro Lett.* **9**(4), 39 (2017). <https://doi.org/10.1007/s40820-017-0196-2>
18. Y. Yang, J. You, Make perovskite solar cells stable. *Nature* **544**(7649), 155 (2017). <https://doi.org/10.1038/544155a>
19. M. Saliba, T. Matsui, K. Domanski, J.Y. Seo, A. Ummadisingu et al., Incorporation of rubidium cations into perovskite solar cells improves photovoltaic performance. *Science* **354**(6309), 5557 (2016). <https://doi.org/10.1126/science.aah5557>
20. J.M. Ball, A. Petrozza, Defects in perovskite-halides and their effects in solar cells. *Nat. Energy* **1**(11), 16149 (2016). <https://doi.org/10.1038/nenergy.2016.149>
21. J. Cheng, H. Zhang, S. Zhang, D. Ouyang, Z. Huang, M.K. Nazeeruddin, J. Hou, W.C. Choy, Highly efficient planar perovskite solar cells achieved by simultaneous defect engineering and formation kinetic control. *J. Mater. Chem. A* **6**(46), 23865 (2018). <https://doi.org/10.1039/C8TA08819E>
22. J.C. Hebig, I. Kühn, J. Flohre, T. Kirchartz, Optoelectronic properties of (CH<sub>3</sub>NH<sub>3</sub>)<sub>3</sub>Sb<sub>2</sub>I<sub>9</sub> thin films for photovoltaic applications. *ACS Energy Lett.* **1**(1), 309–314 (2016). <https://doi.org/10.1021/acsenenergylett.6b00170>
23. T. Singh, A. Kulkarni, M. Ikegami, T. Miyasaka, Effect of electron transporting layer on bismuth-based lead-free perovskite (CH<sub>3</sub>NH<sub>3</sub>)<sub>3</sub>Bi<sub>2</sub>I<sub>9</sub> for photovoltaic applications. *ACS Appl. Mater. Interfaces.* **8**(23), 14542–14547 (2016). <https://doi.org/10.1021/acsami.6b02843>
24. J. You, L. Meng, T.B. Song, T.F. Guo, Y.M. Yang et al., Improved air stability of perovskite solar cells via solution-processed metal oxide transport layers. *Nat. Nanotech.* **11**(1), 75–81 (2016). <https://doi.org/10.1038/nnano.2015.230>
25. W. Liao, D. Zhao, Y. Yu, C.R. Grice, C. Wang et al., Lead-free inverted planar formamidinium tin triiodide perovskite solar cells achieving power conversion efficiencies up to 6.22%. *Adv. Mater.* **28**(42), 9333–9340 (2016). <https://doi.org/10.1002/adma.201602992>
26. H. Tsai, W. Nie, J.C. Blancon, C.C. Stoumpos, R. Asadpour et al., High-efficiency two-dimensional ruddlesden-popper perovskite solar cells. *Nature* **536**(7616), 312–316 (2016). <https://doi.org/10.1038/nature18306>
27. F. Matteocci, L. Cinà, E. Lamanna, S. Cacovich, G. Divitini, P.A. Midgley, C. Ducati, A.D. Carlo, Encapsulation for long-term stability enhancement of perovskite solar cells. *Nano Energy* **30**, 162–172 (2016). <https://doi.org/10.1016/j.nanoen.2016.09.041>
28. G. Flora, D. Gupta, A. Tiwari, Toxicity of lead: a review with recent updates. *Interdiscip. Toxicol.* **5**(2), 47–58 (2012). <https://doi.org/10.2478/v10102-012-0009-2>
29. L. Liang, P. Gao, Lead-free hybrid perovskite absorbers for viable application: can we eat the cake and have it too. *Adv. Sci.* **5**(2), 1700331 (2018). <https://doi.org/10.1002/advs.201700331>
30. F. Hao, C.C. Stoumpos, R.P.H. Chang, M.G. Kanatzidis, Anomalous band gap behavior in mixed Sn and Pb perovskites enables broadening of absorption spectrum in solar cells. *J. Am. Chem. Soc.* **136**(22), 8094–8099 (2014). <https://doi.org/10.1021/ja5033259>
31. T. Krishnamoorthy, H. Ding, C. Yan, W.L. Leong, T. Baikie et al., Lead-free germanium iodide perovskite materials for photovoltaic applications. *J. Mater. Chem. A* **3**(47), 23829–23832 (2015). <https://doi.org/10.1039/C5TA05741H>
32. H. Wang, H. Zhang, C.C. Chueh, T. Zhao, C. Mao, W. Chen, A.K.Y. Jenac, Enhanced crystallization and performance of formamidinium lead triiodide perovskite solar cells through PbI<sub>2</sub>-SrCl<sub>2</sub> modulation. *Mater. Today Energy* **7**, 239 (2018). <https://doi.org/10.1016/j.mtener.2017.10.002>
33. M.T. Klug, A. Osherov, A.A. Haghghirad, S.D. Stranks, P.R. Brown et al., Tailoring metal halide perovskites through metal substitution: influence on photovoltaic and material properties. *Energy Environ. Sci.* **10**(1), 236 (2017). <https://doi.org/10.1039/C6EE03201J>
34. J. Jin, H. Li, C. Chen, B. Zhang, L. Xu, B. Dong, H. Song, Q. Dai, Enhanced performance of perovskite solar cells with zinc chloride additives. *ACS Appl. Mater. Interfaces.* **9**(49), 42875–42882 (2017). <https://doi.org/10.1021/acsami.7b15310>
35. Q. Chen, L. Chen, F.Y. Ye, T. Zhao, F. Tang et al., Ag-incorporated organic-inorganic perovskite films and planar heterojunction solar cells. *Nano Lett.* **17**(5), 3231–3237 (2017). <https://doi.org/10.1021/acs.nanolett.7b00847>
36. J. Zhang, M. Shang, P. Wang, X. Huang, J. Xu, Z. Hu, Y. Zhu, L. Han, n-Type doping and energy states tuning in CH<sub>3</sub>NH<sub>3</sub>Pb<sub>1-x</sub>Sb<sub>2x/3</sub>I<sub>3</sub> perovskite solar cells. *ACS Energy Lett.* **1**(3), 535–541 (2016). <https://doi.org/10.1021/acsenenergylett.6b00241>
37. Y. Hu, T. Qiu, F. Bai, X. Miao, S. Zhang, Enhancing moisture-tolerance and photovoltaic performances of FAPbI<sub>3</sub> by bismuth incorporation. *J. Mater. Chem. A* **5**(48), 25258–25265 (2017). <https://doi.org/10.1039/C7TA08824H>

38. F. Wei, Z. Deng, S. Sun, F. Xie, G. Kieslich, D.M. Evans, M.A. Carpenter, P.D. Bristowe, A.K. Cheetham, The synthesis, structure and electronic properties of a lead-free hybrid inorganic-organic double perovskite  $(\text{MA})_2\text{KBiCl}_6$  (MA = methylammonium). *Mater. Horiz.* **3**(4), 328–332 (2016). <https://doi.org/10.1039/C6MH00053C>
39. P.D. Matthews, D.J. Lewis, P. O'Brien, Updating the road map to metal-halide perovskites for photovoltaics. *J. Mater. Chem. A* **5**(33), 17135–17150 (2017). <https://doi.org/10.1039/C7TA04544A>
40. F. Giustino, H.J. Snaith, Toward lead-free perovskite solar cells. *ACS Energy Lett.* **1**(6), 1233–1240 (2016). <https://doi.org/10.1021/acseenergylett.6b00499>
41. K.W. Bagnall, J.B. Laidler, M.A.A. Stewart, Americium chloro-complexes. *J. Chem. Soc. A* **0**, 133–136 (1968). <https://doi.org/10.1039/J19680000133>
42. L.R. Morss, J. Fuger, Preparation and crystal structures of dicesium berkelium hexachloride and dicesium sodium berkelium hexachloride. *Inorg. Chem.* **8**(7), 1433–1439 (1969). <https://doi.org/10.1021/ic50077a013>
43. L.R. Morss, M. Siegal, L. Stenger, N. Edelstein, Preparation of cubic chloro complex compounds of trivalent metals:  $\text{Cs}_2\text{NaMCl}_6$ . *Inorg. Chem.* **9**(7), 1771–1775 (1970). <https://doi.org/10.1021/ic50089a034>
44. L.R. Morss, W.R. Robinson, Crystal structure of  $\text{Cs}_2\text{NaBiCl}_6$ . *Acta Crystallogr. B* **28**(2), 653–654 (1972). <https://doi.org/10.1107/S0567740872002948>
45. F. Prokert, K.S. Aleksandrov, Neutron scattering studies on phase transition and phonon dispersion in  $\text{Cs}_2\text{NaBiCl}_6$ . *Phys. Status Solidi B* **124**(2), 503 (1984). <https://doi.org/10.1002/pssb.2221240208>
46. W.M.A. Smit, G.J. Dirksen, D.J. Stufkens, Infrared and Raman spectra of the elpasolites  $\text{Cs}_2\text{NaSbCl}_6$  and  $\text{Cs}_2\text{NaBiCl}_6$ : evidence for a pseudo Jahn-Teller distorted ground state. *J. Phys. Chem. Solids* **51**(2), 189–196 (1990). [https://doi.org/10.1016/0022-3697\(90\)90092-T](https://doi.org/10.1016/0022-3697(90)90092-T)
47. I.N. Flerov, M.V. Gorev, K.S. Aleksandrov, A. Tressaud, J. Grannec, M. Couzi, Phase transitions in elpasolites (ordered perovskites). *Mater. Sci. Eng.* **24**(3), 81–151 (1998). [https://doi.org/10.1016/S0927-796X\(98\)00015-1](https://doi.org/10.1016/S0927-796X(98)00015-1)
48. E.T. McClure, M.R. Ball, W. Windl, P.M. Woodward,  $\text{Cs}_2\text{AgBiX}_6$  (X = Br, Cl): new visible light absorbing, lead-free halide perovskite semiconductors. *Chem. Mater.* **28**(5), 1348–1354 (2016). <https://doi.org/10.1021/acs.chemmater.5b04231>
49. G. Volonakis, M.R. Filip, A.A. Haghighirad, N. Sakai, B. Wenger, H.J. Snaith, F. Giustino, Lead-free halide double perovskites via heterovalent substitution of noble metals. *J. Phys. Chem. Lett.* **7**(7), 1254–1259 (2016). <https://doi.org/10.1021/acs.jpcllett.6b00376>
50. Y. Bekenstein, J.C. Dahl, J. Huang, W.T. Osowiecki, J.K. Swabeck, E.M. Chan, P. Yang, A.P. Alivisatos, The making and breaking of lead-free double perovskite nanocrystals of cesium silver-bismuth halide compositions. *Nano Lett.* **18**(6), 3502 (2018). <https://doi.org/10.1021/acs.nanolett.8b00560>
51. S.E. Creutz, E.N. Crites, M.C. De Siena, D.R. Gamelin, Colloidal nanocrystals of lead-free double-perovskite (elpasolite) semiconductors: synthesis and anion exchange to access new materials. *Nano Lett.* **18**(2), 1118 (2018). <https://doi.org/10.1021/acs.nanolett.7b04659>
52. A.H. Slavney, T. Hu, A.M. Lindenberg, H.I. Karunadasa, A bismuth-halide double perovskite with long carrier recombination lifetime for photovoltaic application. *J. Am. Chem. Soc.* **138**(7), 2138–2141 (2016). <https://doi.org/10.1021/jacs.5b13294>
53. Y. Bi, E.M. Hutter, Y. Fang, Q. Dong, J. Huang, T.J. Savenije, Charge carrier lifetimes exceeding 15  $\mu\text{s}$  in methylammonium lead iodide single crystals. *J. Phys. Chem. Lett.* **7**(5), 923–928 (2016). <https://doi.org/10.1021/acs.jpcllett.6b00269>
54. W. Pan, H. Wu, J. Luo, Z. Deng, C. Ge et al.,  $\text{Cs}_2\text{AgBiBr}_6$  single-crystal X-ray detectors with a low detection limit. *Nat. Photonics* **11**(11), 726–732 (2017). <https://doi.org/10.1038/s41566-017-0012-4>
55. R.L.Z. Hoye, L. Eyre, F. Wei, F. Brivio, A. Sadhanala et al., Fundamental carrier lifetime exceeding 1  $\mu\text{s}$  in  $\text{Cs}_2\text{AgBiBr}_6$  double perovskite. *Adv. Mater. Interfaces* **5**(15), 1800464 (2018). <https://doi.org/10.1002/admi.201800464>
56. L. Zhou, Y.F. Xu, B.X. Chen, D.B. Kuang, C.Y. Su, Synthesis and photocatalytic application of stable lead-free  $\text{Cs}_2\text{AgBiBr}_6$  perovskite nanocrystals. *Small* **14**(11), 1703762 (2018). <https://doi.org/10.1002/smll.201703762>
57. A.H. Slavney, L. Leppert, D. Bartesaghi, A. Gold-Parker, M.F. Toney, T.J. Savenije, J.B. Neaton, H.I. Karunadasa, Defect-induced band-edge reconstruction of a bismuth-halide double perovskite for visible-light absorption. *J. Am. Chem. Soc.* **139**(14), 5015–5018 (2017). <https://doi.org/10.1021/jacs.7b01629>
58. K.Z. Du, W. Meng, X. Wang, Y. Yan, D.B. Mitzi, Band-gap engineering of lead-free double perovskite  $\text{Cs}_2\text{AgBiBr}_6$  through trivalent metal alloying. *Angew. Chem. Int. Ed.* **56**(28), 8158–8274 (2017). <https://doi.org/10.1002/anie.201703970>
59. T.T. Tran, J.R. Panella, J.R. Chamorro, J.R. Morey, T.M. McQueen, Designing indirect-direct bandgap transitions in double perovskites. *Mater. Horiz.* **4**(4), 688–693 (2017). <https://doi.org/10.1039/C7MH00239D>
60. G. Volonakis, A.A. Haghighirad, R.L. Milot, W.H. Sio, M.R. Filip et al.,  $\text{Cs}_2\text{InAgCl}_6$ : a new lead-free halide double perovskite with direct band gap. *J. Phys. Chem. Lett.* **8**(4), 772–778 (2017). <https://doi.org/10.1021/acs.jpcllett.6b02682>
61. J. Luo, S. Li, H. Wu, Y. Zhou, Y. Li et al.,  $\text{Cs}_2\text{AgInCl}_6$  double perovskite single crystals: parity forbidden transitions and their application for sensitive and fast UV photodetectors. *ACS Photonics* **5**(2), 398–405 (2017). <https://doi.org/10.1021/acsphotonics.7b00837>
62. N. Nandha, A. Nag, Synthesis and luminescence of Mn-doped  $\text{Cs}_2\text{AgInCl}_6$  double perovskites. *Chem. Comm.* **54**(41), 5205–5208 (2018). <https://doi.org/10.1039/C8CC01982G>
63. K. Tanaka, T. Takahashi, T. Ban, T. Kondo, K. Uchida, N. Miura, Comparative study on the excitons in lead-halide-based perovskite-type crystals  $\text{CH}_3\text{NH}_3\text{PbBr}_3$ ,  $\text{CH}_3\text{NH}_3\text{PbI}_3$ .

- Solid State Commun. **127**(9–10), 619–623 (2003). [https://doi.org/10.1016/S0038-1098\(03\)00566-0](https://doi.org/10.1016/S0038-1098(03)00566-0)
64. C. Zhang, L. Gao, S. Teo, Z. Guo, Z. Xu, S. Zhao, T. Ma, Design of a novel and highly stable lead-free  $\text{Cs}_2\text{NaBiI}_6$  double perovskite for photovoltaic application. *Sustainable Energy Fuels* **2**(11), 2419 (2018). <https://doi.org/10.1039/C8SE00154E>
65. X.G. Zhao, J.H. Yang, Y. Fu, D. Yang, Q. Xu, L. Yu, S.H. Wei, L. Zhang, Design of lead-free inorganic halide perovskites for solar cells via cation-transmutation. *J. Am. Chem. Soc.* **139**(7), 2630–2638 (2017). <https://doi.org/10.1021/jacs.6b09645>
66. T. Li, X. Zhao, D. Yang, M.H. Du, L. Zhang, Intrinsic defect properties in halide double perovskites for optoelectronic applications. *Phys. Rev. Appl.* **10**(4), 41001 (2018). <https://doi.org/10.1103/PhysRevApplied.10.041001>
67. X.G. Zhao, D. Yang, J.C. Ren, Y. Sun, Z. Xiao, L. Zhang, Rational design of halide double perovskites for optoelectronic applications. *Joule* **2**(9), 1662 (2018). <https://doi.org/10.1016/j.joule.2018.06.017>
68. Q. Xu, D. Yang, J. Lv, Y.Y. Sun, L. Zhang, Perovskite solar absorbers: materials by design. *Small Methods* **2**(5), 1700316 (2018). <https://doi.org/10.1002/smt.201700316>
69. X.G. Zhao, D. Yang, Y. Sun, T. Li, L. Zhang, L. Yu, A. Zunger, Cu-In halide perovskite solar absorbers. *J. Am. Chem. Soc.* **139**(19), 6718–6725 (2017). <https://doi.org/10.1021/jacs.7b02120>
70. Z.W. Xiao, K.Z. Du, W.W. Meng, J.B. Wang, D.B. Mitzi, Y.F. Yan, Intrinsic instability of  $\text{Cs}_2\text{In(I)M(III)X}_6$  ( $\text{M}=\text{Bi, Sb}$ ;  $\text{X}=\text{Halogen}$ ) double perovskites: a combined density functional theory and experimental study. *J. Am. Chem. Soc.* **139**(17), 6054–6057 (2017). <https://doi.org/10.1021/jacs.7b02227>
71. M.G. Brik, I.V. Kityk, Modeling of lattice constant and their relations with ionic radii and electronegativity of constituting ions of  $\text{A}_2\text{XY}_6$  cubic crystals ( $\text{A}=\text{K, Cs, Rb, Tl}$ ;  $\text{X}=\text{tetravalent cation}$ ,  $\text{Y}=\text{F, Cl, Br, I}$ ). *J. Phys. Chem. Solids* **72**(11), 1256–1260 (2011). <https://doi.org/10.1016/j.jpcs.2011.07.016>
72. A.E. Maughan, A.M. Ganose, M.M. Bordelon, E.M. Miller, D.O. Scanlon, J.R. Neilson, Defect tolerance to intolerance in the vacancy-ordered double perovskite semiconductors  $\text{Cs}_2\text{SnI}_6$  and  $\text{Cs}_2\text{TeI}_6$ . *J. Am. Chem. Soc.* **138**(27), 8453–8464 (2016). <https://doi.org/10.1021/jacs.6b03207>
73. A.E. Maughan, A.M. Ganose, A.M. Candia, J.T. Granger, D.O. Scanlon, J.R. Neilson, Anharmonicity and octahedral tilting in hybrid vacancy-ordered double perovskites. *Chem. Mater.* **30**(2), 472–482 (2018). <https://doi.org/10.1021/acs.chemmater.7b04516>
74. B. Lee, C.C. Stoumpos, N. Zhou, F. Hao, C. Malliakas, C.Y. Yeh, T.J. Marks, M.G. Kanatzidis, R.P.H. Chang, Air-stable molecular semiconducting iodosalts for solar cell applications:  $\text{Cs}_2\text{SnI}_6$  as a hole conductor. *J. Am. Chem. Soc.* **136**(43), 15379–15385 (2014). <https://doi.org/10.1021/ja508464w>
75. S. Ghosh, S. Paul, S.K. De, Control synthesis of air-stable morphology tunable Pb-free  $\text{Cs}_2\text{SnI}_6$  perovskite nanoparticles and their photodetection properties. *Part. Part. Syst. Char.* **35**(9), 1800199 (2018). <https://doi.org/10.1002/ppsc.20180199>
76. A. Wang, X. Yan, M. Zhang, S. Sun, M. Yang, W. Shen, X. Pan, P. Wang, Z. Deng, Controlled synthesis of lead-free and stable perovskite derivative  $\text{Cs}_2\text{SnI}_6$  nanocrystals via a facile hot-injection process. *Chem. Mater.* **28**(22), 8132–8140 (2016). <https://doi.org/10.1021/acs.chemmater.6b01329>
77. Z. Tan, J. Li, C. Zhang, Z. Li, Q. Hu et al., Highly efficient blue-emitting Bi-doped  $\text{Cs}_2\text{SnCl}_6$  perovskite variant: photoluminescence induced by impurity doping. *Adv. Funct. Mater.* **28**(29), 1801131 (2018). <https://doi.org/10.1002/adfm.201801131>
78. N. Sakai, A.A. Haghghirad, M.R. Filip, P.K. Nayak, S. Nayak et al., Solution-processed cesium hexabromopalladate(IV),  $\text{Cs}_2\text{PdBr}_6$ , for optoelectronic applications. *J. Am. Chem. Soc.* **139**(17), 6030–6033 (2017). <https://doi.org/10.1021/jacs.6b13258>
79. L. Zhou, J.F. Liao, Z.G. Huang, X.D. Wang, Y.F. Xu, H.Y. Chen, D.B. Kuang, C.Y. Su, All-inorganic lead-free  $\text{Cs}_2\text{PdX}_6$  ( $\text{X}=\text{Br, I}$ ) perovskite nanocrystals with single unit cell thickness and high stability. *ACS Energy Lett.* **3**(10), 2613–2619 (2018). <https://doi.org/10.1021/acseenergylett.8b01770>
80. K.F. Guenther, The preparation of some alkali hexabromotitanates (IV). *Inorg. Chem.* **3**(12), 1788–1789 (1964). <https://doi.org/10.1021/ic50022a033>
81. M.G. Ju, M. Chen, Y. Zhou, H.F. Garces, J. Dai et al., Earth-abundant nontoxic titanium (IV)-based vacancy-ordered double perovskite halides with tunable 1.0 to 1.8 eV bandgaps for photovoltaic applications. *ACS Energy Lett.* **3**(2), 297–304 (2018). <https://doi.org/10.1021/acseenergylett.7b01167>
82. Z. Deng, F. Wei, S. Sun, G. Kieslich, A.K. Cheetham, P.D. Bristowe, Exploring the properties of lead-free hybrid double perovskites using a combined computational-experimental approach. *J. Mater. Chem. A* **4**(31), 12025–12029 (2016). <https://doi.org/10.1039/C6TA05817E>
83. F.X. Wei, Z.Y. Deng, S.J. Sun, F.H. Zhang, D.M. Evans et al., Synthesis and properties of a lead-free hybrid double perovskite:  $(\text{CH}_3\text{NH}_3)_2\text{AgBiBr}_6$ . *Chem. Mater.* **29**(3), 1089–1094 (2017). <https://doi.org/10.1021/acs.chemmater.6b03944>
84. Y.J. Li, T. Wu, L. Sun, R.X. Yang, L. Jiang et al., Lead-free and stable antimony-silver-halide double perovskite  $(\text{CH}_3\text{NH}_3)_2\text{AgSbI}_6$ . *RSC Adv.* **7**(56), 3517–35180 (2017). <https://doi.org/10.1039/C7RA06130G>
85. P. Cheng, T. Wu, Y. Li, L. Jiang, W. Deng, K. Han, Combining theory and experiment in the design of a lead-free  $(\text{CH}_3\text{NH}_3)_2\text{AgBiI}_6$  double perovskite. *New J. Chem.* **41**, 9598–9601 (2017). <https://doi.org/10.1039/C7NJ02365K>
86. Z. Deng, F. Wei, F. Brivio, Y. Wu, S. Sun, P.D. Bristowe, A.K. Cheetham, Synthesis and characterization of the rare-earth hybrid double perovskites:  $(\text{CH}_3\text{NH}_3)_2\text{KGDCl}_6$  and  $(\text{CH}_3\text{NH}_3)_2\text{KYCl}_6$ . *J. Phys. Chem. Lett.* **8**(20), 5015–5020 (2017). <https://doi.org/10.1021/acs.jpcclett.7b02322>



87. T.T. Tran, M.A. Quintero, K.E. Arpino, Z.A. Kelly, J.R. Panella, X. Wang, T.M. McQueen, Chemically controlled crystal growth of  $(\text{CH}_3\text{NH}_3)_2\text{AgInBr}_6$ . *CrystEngComm* **20**, 5929–5934 (2018). <https://doi.org/10.1039/C8CE00702K>
88. F. Funabiki, Y. Toda, H. Hosono, Optical and electrical properties of perovskite variant  $(\text{CH}_3\text{NH}_3)_2\text{SnI}_6$ . *J. Phys. Chem. C* **122**(20), 10749 (2018). <https://doi.org/10.1021/acs.jpcc.8b01820>
89. W. Meng, X. Wang, Z. Xiao, J. Wang, D.B. Mitzi, Y.J. Yan, Parity-forbidden transitions and their impact on the optical absorption properties of lead-free metal halide perovskites and double perovskites. *J. Phys. Chem. Lett.* **8**(13), 2999–3007 (2017). <https://doi.org/10.1021/acs.jpcclett.7b01042>
90. L.Z. Lei, Z.F. Shi, Y. Li, Z.Z. Ma, F. Zhang et al., High-efficiency and air-stable photodetectors based on lead-free double perovskite  $\text{Cs}_2\text{AgBiBr}_6$  thin films. *J. Mater. Chem. C* **6**(30), 7982–7988 (2018). <https://doi.org/10.1039/C8TC02305K>
91. C. Wu, B. Du, W. Luo, Y. Liu, T. Li et al., Highly efficient and stable self-powered ultraviolet and deep-blue photodetector based on  $\text{Cs}_2\text{AgBiBr}_6/\text{SnO}_2$  heterojunction. *Adv. Optical Mater.* (2018). <https://doi.org/10.1002/adom.201800811>
92. H. Li, X. Shan, J.N. Neu, T. Geske, M. Davis, P. Mao, K. Xiao, T. Siegrist, Z. Yu, Lead-free halide double perovskite-polymer composites for flexible X-ray imaging. *J. Mater. Chem. C* **6**, 11961–11967 (2018). <https://doi.org/10.1039/C8TC01564C>
93. Q. Hu, Z. Deng, M. Hu, A. Zhao, Y. Zhang, Z. Tan, G. Niu, H. Wu, J. Tang, X-ray scintillation in lead-free double perovskite crystals. *Sci. China Chem.* **61**, 1 (2018). <https://doi.org/10.1007/s11426-018-9308-2>
94. J. Luo, X. Wang, S. Li, J. Liu, Y. Guo et al., Efficient and stable emission of warm-white light from lead-free halide double perovskites. *Nature* **563**, 541–545 (2018). <https://doi.org/10.1038/s41586-018-0691-0>
95. F. Moser, S. Lyu, Luminescence in pure and I-doped  $\text{AgBr}$  crystals. *J. Lumin.* **3**(6), 447–458 (1971). [https://doi.org/10.1016/0022-2313\(71\)90025-1](https://doi.org/10.1016/0022-2313(71)90025-1)
96. E. Greul, M.L. Petrus, A. Binek, P. Docampo, T. Bein, Highly stable, phase pure  $\text{Cs}_2\text{AgBiBr}_6$  double perovskite thin films for optoelectronic applications. *J. Mater. Chem. A* **5**(37), 19972–19981 (2017). <https://doi.org/10.1039/C7TA06816F>
97. C. Wu, Q. Zhang, Y. Liu, W. Luo, X. Guo et al., The dawn of lead-free perovskite solar cell: highly stable double perovskite  $\text{Cs}_2\text{AgBiBr}_6$  film. *Adv. Sci.* **5**(3), 1700759 (2018). <https://doi.org/10.1002/advs.201700759>
98. W. Gao, C. Ran, J. Xi, B. Jiao, W. Zhang, M. Wu, X. Hou, Z. Wu, Quality  $\text{Cs}_2\text{AgBiBr}_6$  double perovskite film for lead-free inverted planar heterojunction solar cells with 2.2% efficiency. *ChemPhysChem* **19**(14), 1696–1700 (2018). <https://doi.org/10.1002/cphc.201800346>
99. M. Pantaler, K.T. Cho, V.I.E. Quelo, I.G. Benito, C. Fettkenhauer et al., Hysteresis-free lead-free double perovskite solar cells by interface engineering. *ACS Energy Lett.* **3**(8), 1781–1786 (2018). <https://doi.org/10.1021/acscenergylett.8b00871>
100. M. Wang, P. Zeng, S. Bai, J. Gu, F. Li, Z. Yang, M. Liu, High-quality sequential-vapor-deposited  $\text{Cs}_2\text{AgBiBr}_6$  thin films for lead-free perovskite solar cells. *Solar RRL* (2018). <https://doi.org/10.1002/solr.201800217>
101. X. Qiu, B. Cao, S. Yuan, X. Chen, Z. Qiu et al., room unstable  $\text{CsSnI}_3$  to air-stable  $\text{Cs}_2\text{SnI}_6$ : a lead-free perovskite solar cell light absorber with bandgap of 1.48 eV and high absorption coefficient. *Sol. Energy Mater. Sol. Cells* **159**, 227–234 (2017). <https://doi.org/10.1016/j.solmat.2016.09.022>
102. X. Qiu, Y. Jiang, H. Zhang, Z. Qiu, S. Yuan, P. Wang, B. Cao, Lead-free mesoscopic  $\text{Cs}_2\text{SnI}_6$  perovskite solar cells using different nanostructured  $\text{ZnO}$  nanorods as electron transport layers. *Phys. Status Solidi (RRL)* **10**(8), 587–591 (2016). <https://doi.org/10.1002/pssr.201600166>
103. B. Lee, A. Krenselewski, S.I. Baik, D.N. Seidman, R.P.H. Chang, Solution processing of air-stable molecular semiconducting iodosalts,  $\text{Cs}_2\text{SnI}_{6-x}\text{Br}_x$ , for potential solar cell applications. *Sustainable Energy Fuels* **1**(4), 710–724 (2017). <https://doi.org/10.1039/C7SE00100B>
104. M. Chen, M.G. Ju, A.D. Carl, Y. Zong, R.L. Grimm et al., Cesium titanium (IV) bromide thin films based stable lead-free perovskite solar cells. *Joule* **2**(3), 558–570 (2018). <https://doi.org/10.1016/j.joule.2018.01.009>
105. Q.A. Akkerman, M. Gandini, F. Di Stasio, P. Rastogi, F. Palazon et al., Strongly emissive perovskite nanocrystal inks for high-voltage solar cells. *Nat. Energy* **2**(2), 16194 (2016). <https://doi.org/10.1038/nenergy.2016.194>
106. Z. Liu, B. Sun, X. Liu, J. Han, H. Ye, T. Shi, Z. Tang, G. Liao, Efficient carbon-based  $\text{CsPbBr}_3$  inorganic perovskite solar cells by using Cu-phthalocyanine as hole transport material. *Nano-Micro Lett.* **10**(2), 34 (2018). <https://doi.org/10.1007/s40820-018-0187-3>
107. Y. Chen, X. Wu, Y. Chu, J. Zhou, B. Zhou, J. Huang, Hybrid field-effect transistors and photodetectors based on organic semiconductor and  $\text{CsPbI}_3$  perovskite nanorods bilayer structure. *Nano-Micro Lett.* **10**(4), 57 (2018). <https://doi.org/10.1007/s40820-018-0210-8>